# Alloying-induced softening in metal nanowires studied by atomistic simulations

**by**

**Zuoyong Zhang**

A Thesis Submitted to the Faculty of Graduate Studies of

The University of Manitoba

in partial fulfillment of the requirements of the degree of

**MASTER OF SCIENCE**

**Department of Mechanical Engineering**

**University of Manitoba**

**Winnipeg, Canada**

# Abstract

To improve the mechanical properties of metal nanowires, alloying is believed to be an effective pathway by adding solute atoms into the host matrix during the fabrication process. In this project, the alloying effects on the mechanical properties and yield mechanisms of metal nanowires have been studied by atomistic simulations. The chemical complexity influence on the softening phenomenon has also been investigated through different alloy systems. The results reveal that softening effects on yield strength can be widely observed in alloy nanowires. The underlying softening sources have been discussed and two major mechanisms have been found: the alloying-induced reduction in stacking fault energy and the increase in atomic size misfit. The weight of two mechanisms on solid solution softening depends on the variation of stacking fault energy and atomic size misfit degree caused by changing the solute concentration, which provides new perspectives to design novel single crystalline metal nanowires.

# Acknowledgements

It is a great honor for me to have a chance to extend my graduate study at the University of Manitoba. I can remember how shocked my colleagues were when I told them that I would leave for further study and resign from the company where I had worked for more than ten years. How time flies! Now, I am going to finish my Master's program. It is an awesome journey during which I have learnt knowledge, made new friends, and got trained about how to perform research work.

Here, I would like to express my sincere appreciation to my supervisor Dr. Chuang Deng, who is a remarkable scholar and gives me the chance to pursue my graduate study at the University of Manitoba. He has profound knowledge of material science and gives me valuable guidance in my study very kindly and patiently. I could not have finished this project without his inspiring instruction. I appreciate what he has done to help me not only in my studies but also in other aspects. He and the faculty also provided me with a chance to work as a teaching assistant, and a fellowship opportunity which both helped me with financial support.

Then, I would like to thank my committee members, Dr. Chuang Deng, Dr. Guozhen Zhu, and Dr. Nan Wu, who all come from the Department of Mechanical Engineering. Thanks a lot for reviewing my thesis, giving valuable comments, and attending my thesis defense.

In addition, I would like to express my appreciation to all the instructors of the

courses that I have taken in the first year of my M.Sc. study. Their instruction has helped me to understand deeper about the knowledge of Nano-material Technology, Molecular Dynamics simulations, Electron Microscope techniques, and phase transformation in solids. I also appreciate the usage of computing resources provided by West Grid and the Digital Research Alliance of Canada.

Finally, I want to express my thanks and love to my family, especially to my wife. Without their encouragement and financial support, I cannot finish my graduate study here. Several years have passed since I decided to study abroad. My wife is the one who always stands by me and gives me support unconditionally.

# Table of Contents

# Table of Figures

# Chapter I Introduction, motivation, and outline of thesis

## 1.1 Introduction

Nowadays, the invention and development of cutting-edge engineering and technologies are highly dependent on the innovation of materials. Inspired by the great statement “there is plenty of room at the bottom”, which was presented by Dr. Richard P. Feynman in 1959 [1], researchers have paid dramatic attention to discover, investigate and develop the so-called nanoscience and nanotechnology in the past decades, which are believed to be the vigorous driving force for the development of various technologies such as food science and agriculture [2], [3], energies [4], [5], and medical science [6].

One of the most important branches of nanotechnologies is one-dimensional (1-D) materials. Those with at least two of their three dimensions less than 100 nm are defined as 1-D structures [7], [8], such as nanopillars, nanoparticles, and nanowires etc. which have been extensively studied due to the outstanding mechanical, magnetic, and electronic properties with respect to the high aspect ratio. In recent years, metal nanowires (MNWs), a crucial 1-D nanostructure, reveal great interests from materials scientists. The perfect electrical and thermal conducting behaviors of MNWs open up comprehensive applications in various fields. Nevertheless, the mechanical properties may have profound influences on their applications. For instance, in some scenarios, higher strength and stiffness of the materials are preferred, while in some other conditions, better elastic property is essential for the proper applications, which leaves us with a critical target of today’s physical metallurgy, that is to improve the properties by means of alloying.

## 1.2 Motivation

In the history of materials, researchers are always diligently focusing on searching for materials with higher strength by manipulating the microstructures, composition, and sizes of the materials. For instance, to realize the dream of going to space by a “space elevator”, the US National Aeronautics and Space Administration (NASA) started a so-called “space tether challenge” in 2005 [9]. The aimed materials should have super high strength and be relatively light in weight. To fulfill this purpose, carbon fibers [10] and polymeric fibers [11] were developed, but none of them could meet the demands. Until 2018, Bai et. al [12] fabricated carbon nanotube bundles with ultra-high strength up to 80 GPa. However, there still has a long way to go in practice.

Alloying, to some extent, is believed to be the classic pathway to improve the mechanical properties of metal materials, especially in yield strength. By adding solute atoms into the host matrix, higher strength is usually expected to be obtained, which is defined as “solid solution hardening” or “solid solution strengthening” [13]. Sometimes, alloying can also facilitate the materials to behave more anti-corrosion, higher electrical and thermal conductivities. Nevertheless, we need the materials to perform with higher toughness but proper strength to avoid fatigue fractures caused by periodic load. For this scenario, alloying can also provide a reliable solution by slightly reducing the strength but improving the toughness of the material. This phenomenon can be described as “solid solution softening”, which is opposite to the strengthening effect aforementioned.

For 1-D materials, such as nanopillars, nanoparticles as well as nanowires, alloying is also a potential method to improve their thermal stability and mechanical properties. For MNWs, the addition of solute atoms may induce different mechanical behaviors compared to conventional bulk materials. However, there is little literature regarding the alloying effects on MNWs, especially the softening effect. Thus, atomistic simulations are employed to investigate the softening effects induced by alloying of various MNWs, and the underlying mechanisms of the softening phenomena.

## 1.3 Outline of the thesis

In Chapter II, a brief history, fabrication methods, and applications will be firstly introduced. Then, the mechanical properties of MNWs will be reviewed based on the previous literatures. In particular, the yield and deformation mechanisms will be highlighted. Finally, the alloy effects on the mechanical properties of metal materials in nano-scale will be reviewed. The strengthening and softening effects and their mechanisms will be outlined in this chapter as well.

The atomistic simulation methods will be introduced in Chapter III. It demonstrates the basic theory and tools of molecular dynamics (MD) simulations, which are employed in this project. The atomic force evaluation methods which are used in this project are also briefly introduced in this chapter. Then, it illustrates the computational details of how to perform the uniaxial tensile tests of different alloy MNWs via MD simulations. To understand the solute distribution effects on the results, Monte Carlo (MC) simulations are also employed which are hybrid with MD processes. The planar fault energy calculations are also elaborated in this section.

The simulation results and discussions are shown in Chapter IV. All the uniaxial tensile results are illustrated in this section, combined with the comparison of solute distribution effects, temperature effects, and size effects on the softening phenomena, followed by the discussions and analyses of softening effects induced by alloying in single crystalline MNWs.

Key conclusions of the atomistic studies are summarized at the end of the thesis, Chapter V. Shortcomings of present work are illustrated and following with future work expectation.

# Chapter II Research background

## 2.1 Introduction of MNWs

### 2.1.1 Brief history of MNWs

Nanowire (NW), similar to other 1-D materials in nano-scale, is generally defined as a wire-like structure with a diameter no more than 100 nm, and unconstrained in length, which determines the ultra-high length-diameter ratio. A quasi-nanowire was firstly developed by the scientists at the famous Bell laboratories in 1987 [14]. Then, the Belgium engineer Jean-Pierre Colinge developed and described the silicon-on-insulator (SOI) technology in 1991, when a more refined nanowire was introduced [15]. Since then, scientists have shown great interest in fabrication, development, and applications of NWs.

When the size of the material is reduced to nano-scale, the properties are expected to be dramatically different from the bulk ones, which can be attributed to the so-called quantum confinement effect. It describes the energy levels, valance band and energy band gap of electrons [16]. But when the material size is comparable to the Bohr radii of electrons, the quantum confinement effects can be observed. Under this circumstance, researchers cast their eyes on the MNWs and expect the mechanical, electrical, and magnetic properties of the MNWs can be observed remarkably different to those of the corresponding bulk materials.

The MNWs were firstly reported to be fabricated by Itoua and Joachim [17]. They successfully obtained gold NWs with width less than 50 nm by lithography method in a glass substrate in 1992. Then, P. M. Ajayan and Sumio Iijima synthesized copper NWs in carbon nanotubes under the capillary force in the next year [18]. In 1993, Whitney et al. reported that they successfully fabricated arrays of Ni and Co NWs by electro-chemical deposition method, and distinctive magnetic properties were characterized by them [19]. Hereafter, MNWs became one of the most popular topics among nanomaterials, and various fabrication methods were thoroughly developed. To date, MNWs have been profoundly used in novel batteries, biomedical sensors, and shape memory devices. Currently, more applications of MNWs are under discovery and development.

### 2.1.2 Fabrication methods of MNWs

The emergence of novel materials is invariably based on the development of fabrication methods. Similar to the other nanomaterials, people have two pathways to choose to synthesize MNWs, in which one is the so-called bottom-up method, another one is the top-down pathway [20], [21]. The former, bottom-up methods start from very small components, probably on an atomic or molecular scale, as the building blocks to grow MNWs on specific substrates or some templates. In contrast, the latter, the top-down methods indicate that MNWs are synthesized from bulk materials by cutting down the unwanted parts by a mold or a mask pattern. Generally, compared to top-down methods, the bottom-up methods are more reliable which is because of the higher controllability in composition distribution, microstructures, and cost [20], [22], [23]. Thus, researchers prefer to use bottom-up methods to fabricate MNWs.

#### 2.1.2.1 Template-assisted methods

One of the low-cost bottom-up methods is the template-based method to synthesize MNWs. As described previously, the earliest MNWs were made by the famous capillary suction force using carbon nanotubes as the template [18]. The lead particles were deposited onto the surface of the carbon nanotube under a high vacuum condition, then the samples were annealed in air atmosphere at 400 °C higher than the melting point of lead. After a while, they found that nanotube was filled with solid metal. Then, carbon nanotubes were used as the reaction templates to synthesize MNWs [24]. To date, more template-based methods have been developed to synthesize MNWs, such as template-assisted electrochemical deposition [25]–[29] and biomolecular templates [30]–[32].

Template-assisted electrodeposition method is a typical growth technique by depositing metals from an electrolyte [28]. This method is reported with low-cost, easy to operate, large area yields and ability for high aspect ratio products (very useful for manufacturing MNWs) [33]. It employs nano-porous anodic aluminum oxide (AAO) or nano-porous alumina as templates [34]. The typical synthesis processes are shown in Figure 1. Generally, the processes can be divided into three steps, AAO pore preparation, conducting membranes (metal) deposition or sputtering on one side, and final MNWs deposition on the other side [28], [29]. The diameter of the production MNWs is defined by the size of the AAO pores which is controllable during the AAO preparation by modifying the aluminum anodization potential or the etching duration [29]. The length of the MNWs can be simply controlled by the deposition duration [28]. Template-assisted electrodeposition not only can be applied to fabricate pure metal NWs, but also can be used to manufacture alloy MNWs. For instance, binary alloy MNWs [35]–[37], ternary alloy MNWs [38], [39], and even MNWs with more elements [40], [41] can be synthesized by template-assisted electrodeposition methods. Therefore, it is a versatile template-based pathway to obtain MNWs for researchers to choose.

This figure has been removed for copyright issue.

**Figure 1**. Schematic of the typical electrodeposition processes of synthesizing MNWs. [29]

Another template-based method is using bio-molecules as the templates such as DNA chins [31], [32], [42], [43] and protein assemblies [44], [45]. Undoubtedly, DNA chains are perfect candidates for templates to synthesize nanomaterials because of the intramolecular and intermolecular properties, such as some special sulfur or nitrogen functional ligands which can interact with metal ions [46]. DNA has already been applied to synthesize various nanomaterials, like nanoparticles, nanorods and nanorings etc. Metal ions can self-assemble into the DNA chains by interacting with the ligands. With the help of some special agents, the metal ions can be reduced to zero valence state metals. Then, free standing MNWs can be obtained by dissolving the samples into proper organic solvents. The diameter of the MNWs can be controlled by adjusting the concentration of metal ions and the duration of interaction between DNA and metal ions [43]. And the length of the MNWs is defined by the length of the DNA chains.

The γ-prefoldin filamentous protein (γ-PFD) was reported that can serve as a proper bio-template candidate for manufacturing nanomaterials [47], [48]. The mechanism is similar to the DNA-based template method. Under some specific conditions, metal ions can be self-assembled onto the protein surface. Then, with the help of reductants, the metal ions can be reduced to MNWs with different conductive properties, but the MNW length is defined by the protein [44].

This figure has been removed for copyright issue.

**Figure 2.** Preparation of Au-Pt core-shell NWs. (a) Schematic illustration of the preparation of the complex MNWs of interest. (b) TEM image of Au-core. (c) TEM image of Au-Pt core-shell structure. (d) UV-Vis characterization of the product. (e) and (f) elemental mapping: Au-red, Ag-blue, Pt-green. (g) shows the mixture of different colors. [49]

In recent years, some plant viruses have been developed as templates for synthesizing nanomaterials [50], [51]. The synthesizing processes are electroless and can be operated in ambient conditions. By mixing the virus solution with the metal ion solution, metal ions can be deposited onto the virus and reduced without any additional agents to form the polydisperse MNWs combined with virus [51]. People can choose to separate the wanted MNWs by using proper solution, but there are more possibilities for researchers to collect the polydisperse product for certain applications. More complex core-shell structures are possible to be fabricated using this method, shown in Figure 2. It shows the complex structure of the NWs. The diameter of NWs is controlled by the size of the virus, and the length is a function of the interaction duration between the metal ions and the virus.

In summary, template-assisted method is an effective, low-cost, high-yield, and easy-operation fabrication pathway to obtain MNWs. the size and structures of the products are well controlled by adjusting the synthesizing parameters. Moreover, it is possible for researchers to fabricate MNWs with complexity both in composition and micros-structures.

#### 2.1.2.2 Other methods

This figure has been removed for copyright issue.

**Figure 3.** Schematic illustration of the fabrication processes of (A) platinum NWs and (B) gold NWs by laser assisted mechanical pulling method. [57]

Although template-assisted methods are effective in synthesizing MNWs, there are some other methods applicable for researchers to choose, such as the chemical vapor deposition (CVD) [52]–[55], laser-assisted methods [56]–[59], nano-lithography [60], [61], and nano-scratching [62]. CVD is a very common, bottom-up, and straightforward pathway to fabricate 1-D nanostructures. It is often used to fabricate semiconductor nanostructures, metal oxide NWs and carbon nanotubes. However, the highly controllable growth properties inspire researchers to develop CVD method in fabricating MNWs. It allows MNWs to grow on silicon substrates [52], [54] and even metal film substrates [53] in large-area free standing style and with a very fast speed.

In recent years, laser-based techniques have drawn dramatical attention from researchers. Undoubtedly, it has been successfully developed to manufacture nanostructures by material scientists [63]. Generally, it is a top-down method, and conventional fabrication methods may be involved, such as lift-off lithography and stretching. In 2014, Percival et al. [57] developed a novel method by using glass to seal a small piece of metal wire and pulled by laser-assisted mechanical puller, shown in Figure 3, until being separated into two ultra-sharp tips. To bare the MNWs, it is very convenient to use hydrofluoric (HF) acid to etch the quartz. The length of the obtained MNWs can be as long as 5-millimeter scale, and the diameter can come to only tens of nanometers. Thus, the MNWs produced by this method have an ultra-high aspect ratio. However, this laser-assisted pulling method has limits in yield amount and multiple steps requiring high accuracy operations. To overcome the complexity of fabrication processes, He et al. [59] developed another laser-assisted direct writing method to fabricate MNWs. They designed a two-beam laser direct writing system, shown in Figure 5. It allows operators to fabricate MNWs by directly writing on a flexible polyethylene terephthalate (PET) sheet for further applications, such as wearable communication devices [64]. The size and morphology of the MNWs are controllable by means of adjusting the experimental conditions. This technique provides high potential for fabricating flexible conductive MNWs for cutting-edge applications.

This figure has been removed for copyright issue.

**Figure 4.** Schematic diagram of the two-beam laser direct writing system. [59]

MNWs can be fabricated by lithography-based methods as well, like the other nanostructures. Nanoimprint lithography (NIL), a conventional fabrication method, has been previously used to produce metal nanorings [65], nanodots [66] and MNWs [67], [68]. One of the obvious merits of this method is the highly ordered products. The fabrication processes are schematically shown as Figure 5. The first step is to spin-coat a thin layer of thermoplastic resist polymer onto the proper substrate, followed by NIL process to form ordered polymer grating. Then, a reactive ion etching (RIE) process is employed to bare the substrate and remove the residual polymer, followed by compression using another substrate to control the groove width and depth. Then, a thin metal layer can be evaporated deposition onto the pattern. Finally, MNWs can be obtained after a lift-off process in acetone solution for proper duration. The size of the MNWs can be easily controlled by adjusting the experimental conditions, such as the compression pressure, duration, and deposition duration. But, the obtained MNWs have a rectangular cross-section with sharp edges, which may affect the mechanical behavior.

This figure has been removed for copyright issue.

**Figure 5.** Schematic illustration of the fabrication processes of MNWs. [68]

In summary, a variety of fabrication methods have been developed to synthesis MNWs, which guarantees progress in the post research. Generally, template-assisted electrodeposition is the most preferred pathway, which can be attributed to the low-cost, high efficiency, ability to produce large area MNWs, and highly controllable in size. However, the two-beam laser direct writing system allows people to fabricate MNWs on soft sheets, which exhibits higher flexibility applications.

### 2.1.3 Applications of MNWs

MNWs have been applied in various fields due to the unique properties, such as high aspect ratio, large surface area, flexibility, and high conductivity. Thanks to the remarkable progress in fabrication methods of MNWs, in the past decades, people are able to fabricate various conventional and novel products for various applications, such as electrodes [26], [69]–[71], sensors [72], [73], waveguides [74], and shape memory [75]–[77]. As described previously, the two-beam laser direct writing method can be used to produce MNWs applied for wearable devices which need both conductivity and flexibility properties of the MNWs [59]. Thus, the development of MNWs in applications is based on the progress in fabrication methods.

This figure has been removed for copyright issue.

**Figure 6.** (a) SEM images of Ag NW networks on a silicon substrate, and the distributions of length and diameter of the NWs. (b) Sheet resistance versus annealing time for the Ag NW networks at 200 °C. (c) Sheet resistance versus NW density. [69]

Transparent conductive electrodes are important parts of solar cells and some display screens. Conventional electrodes use doped metal oxides, which may impede the light signals to pass through, have higher electrical resistance and exhibit brittleness. To overcome those drawbacks of conventional electrodes, researchers developed novel electrodes based on MNW networks [69]–[71]. The typical configuration of this kind of electrodes are shown in Figure 6 (a). It also shows the relationship between sheet resistance and annealing time Figure 6 (b), and the sheet resistance against NW density Figure 6 (c). Thus, MNW network electrodes are a great replacement for conventional metal oxide-based ones. MNWs can be used as sensors to detect such as biomolecules [78], chemicals [72], [79] and strains in multidimensions [80], where different properties are adopted.

This figure has been removed for copyright issue.

**Figure 7.** (a) Initial structure of <5 5 2>-oriented gold NW. (b) The nucleation and propagation of nano twinning, and the NW reorientation under tensile loading. (c) Reverse reorientation of the NW by compression. [77]

The rubber-like pseudoelastic property of copper NWs was first found by atomistic simulations by Liang and Zhou in 2005 [81]. Thereafter, pseudoelasticity and shape memory effects have drawn remarkable attention from researchers. To date, shape memory effects have been verified in both single crystalline FCC [77] and BCC MNWs [75]. The pseudoelastic behavior refers that the materials exhibit rubber-like and recover to initial condition by inverse load, which is shown in Figure 7. The revisable behavior is believed due to the reorientations of the crystallographic lattice by twin boundary motion near the sliding planes [77], [81]. Similar pseudoelasticity and shape memory effects are also found in body-centered-cubic (bcc) structured MNWs [75]. The phenomenon can be attributed to the transition from twinning to detwinning, which behaves like face-centered-cubic (fcc) MNWs. Shape memory is an important application of MNWs, which is usually used to store energy and damp the vibration.

## 2.2 Mechanical properties and deformation mechanisms of MNWs

### 2.2.1 Mechanical properties of metals

This figure has been removed for copyright issue.

**Figure 8.** Schematic representation of a standard metal specimen for tensile testing. [82]

This figure has been removed for copyright issue.

**Figure 9.** Schematic representation of a tensile testing apparatus. [82]

For many materials, they are always exposed to various loads, while in service, such as the steel bars used for buildings and aluminum alloy rims mounted on vehicles. However, improper design of materials may probably cause terrible disasters, for instance air crash, bridge collapse and furnace explosion. Thus, it is crucial to understand the physical meaning of the various mechanical properties of materials and be clear about how they are examined. After that, it is possible for engineers to design different products based on the knowledge of the properties of materials, especially metals. The products should meet the demands of expectations for engineering applications.

To understand the mechanical properties of metals, some concepts need to be introduced. To simplify, the applied loads on materials may be described as three pure types, which are tension, compression, and shear, although the loading conditions might be much more complex in practice. For engineering materials, strength is always the concern of engineers. Several testing methods have been developed to obtain the strength of engineering materials, among which tensile test is one of the most common techniques.

In the early days, people found the size effects on material strength based on the tensile tests. Thus, tensile strength measurement standards have been developed to define how to perform tensile tests. A standard metal specimen for tensile testing looks like a dog-bone, shown in Figure 8. Normally, the cross-section of the specimen is circular with a defined diameter of ~0.5 inch, and the reduced section length should be at least 4 times of the cross-section diameter. The gauge length, approximately 2 inches, is used to measure the elongation of the specimen under uniaxial tensile load.

A fundamental apparatus for conducting tensile tests are shown in Figure 9. Two ends of the specimen are grasped by clamps, and the load is applied by moving the crosshead, while the load and elongation can be recorded by a computer. According to the recorded data, a stress-strain curve can be obtained, where stress describes the interactions between particles and strain refers to the elongation ratio in general. Without considering the shrink of the sample's cross-section, the obtained stress $\sigma$ is defined as the engineering stress, shown as Eq (1), where $F$ is the applied force, and $A_0$ is the original cross-section area. Under this circumstance, the strain $\varepsilon$ is defined as the engineering strain, which is a unitless physical value, described as Eq (2), where $l_i$ is the measured length of the sample, and $l_0$ is the original length.

$$\sigma = \frac{F}{A_0} \qquad \text{Eq (1)}$$

$$\varepsilon = \frac{l_i - l_0}{l_0} \qquad \text{Eq (2)}$$

True stress and strain are the counterparts of engineering ones, in which true stress, marked as $\sigma_T$, is defined as the load $F$ over the instantaneous cross-section area $A_i$, shown as Eq (3). Moreover, the true strain $\varepsilon_T$ is defined as the logarithm of the ratio instantaneous length $l_i$ over the original length $l_0$, shown as Eq (4).

$$\sigma_T = \frac{F}{A_i} \qquad \text{Eq (3)}$$

$$\varepsilon_T = \ln \frac{l_i}{l_0} \qquad \text{Eq (4)}$$

This figure has been removed for copyright issue.

**Figure 10.** A typical stress-strain curve of a low carbon steel. [83]

A typical stress-strain curve of a low carbon steel is shown in Figure 10. There is an elastic regime, where stress linearly increases with strain, until the yield point where the stress is named yield strength. In this region, the deformation of the specimen is reversible, and no permanent deformation is observed. The relationship between stress $\sigma$ and strain $\varepsilon$ describes as *Hooke's law*, shown as Eq (5):

$$\sigma = E\varepsilon \qquad \text{Eq (5)}$$

where, $E$ is the slope of the curve in the linear region, named as elastic modulus, or Young's modulus. Sometimes, Young's modulus is described as the stiffness of material. Higher Young's modulus means stiffer of the material. Thereafter, the stress increases with strain non-linearly, until reaching the highest point which is defined as the ultimate strength. This region is called strain hardening. In this region, plastic deformation dominates, which means the deformation is permanent, and non-reversible. After reaching the ultimate strength, the specimen starts necking until fracture occurs.

Another important mechanical property is ductility, which is used to describe the ability of the material to sustain plastic deformation before fracture. There are two expressions of ductility, which are the percentage of elongation, $\%EL$, and the percentage of reduction in area, $\%RA$. The former, the percentage of elongation, is defined as Eq (6):

$$\%EL = \frac{l_f - l_0}{l_0} \times 100 \qquad \text{Eq (6)}$$

where, $l_f$ is the length of specimen at fracture. The expression of ductility in percentage of reduction in area is defined as Eq (7):

$$\%RA = \frac{A_0 - A_f}{A_0} \times 100 \qquad \text{Eq (7)}$$

where, $A_f$ is the cross-sectional area at fracture. A higher ductility value means the material is ductile under load. In contrast, a low ductility value indicates the brittleness of material. Generally, when the fracture strain is less than 5%, the material is defined as brittle material [82], such as glass, cast iron and ceramics.

The mechanical properties aforesaid are related to tensile load conditions. Nevertheless, metals may experience other loads in practice, such as compression, torsion, and shearing. The mechanical properties of these loads are similar to the tensile ones. But there is no maximum deformation under compression since there is no necking phenomenon. The apparatus for tensile tests, shown in Figure 9, can be used to perform compression tests as well, by transforming the tensile loads to compressive ones. Similarly, shear stress is defined as shear force over the shear area. The shear strain is defined as the tangent of the strain angle, which is different from the strains of tension and compression. Generally, all these testing techniques are well defined by standard.

### 2.2.2 Mechanical properties of MNWs

For MNWs, the mechanical properties are defined the same as other metal materials. However, it is a tough mission to measure the mechanical properties of MNWs, since they are nano-scale. It is really challenging to fix both ends of a single MNW and apply force then.

Owing to the progress of electron microscopic techniques, such as Transmission Electron Microscopy (TEM) and Scanning Electron Microscopy (SEM), it is possible to perform in-situ experiments to examine the mechanical properties of a single MNW. Compared to experimental methods, simulations also draw plenty of interest from researchers in characterizing the mechanical properties of MNWs, due to the advantages of high manipulation, low-cost and fast observation. It allows researchers to observe all the detail, such as dislocation nucleation, propagation, and deformation mechanisms, by dumping snapshots during the simulation process. In this section, characterization of the mechanical properties of MNWs will be reviewed in both experiments and simulations.

### 2.2.2.1 In-situ experiments

Conventional testing techniques, for instance tension, compression and shear testing methods described previously, are inapplicable for individual MNW testing, since they are extremely small in size, and challenging in fixing and applying nano-mechanical load. In-situ uniaxial tensile testing is a widely used method to examine the mechanical properties of MNWs practically. In the past two decades, researchers performed a lot of in-situ tensile experiments to measure the strength and Young's modulus of various MNWs.

This figure has been removed for copyright issue.

**Figure 11.** (a) An in-situ SEM tensile testing device set-up. (b) SEM image showing the fracture surface of the examined Ag NW. [84]

A typical in-situ tensile testing experiment is shown in Figure 11, which was performed by Zhu et al. [84]. The nano-mechanical device is composed of an AFM cantilever and a nanomanipulator, which was successfully used in their previous work on semiconductor NWs [85], [86]. Two ends of the MNW are fixed on the nano-manipulator and atomic force microscopy (AFM) cantilever, respectively, by using the electron-beam-induced deposition of carbonaceous materials in the SEM [85]. Then, a nano-mechanical tensile load can be applied to the specimen until fracture. During the tensile test, SEM images can be taken to observe the evolution of strain, force, and the deformation behavior. With the help of this device, they found the size dependence of five-twinned Ag NWs, with the result of the smaller in diameter, the stronger in strength, which can be attributed to the surface effect of the MNWs.

This figure has been removed for copyright issue.

**Figure 12.** (a) Schematic illustration of a three-point indentation device for measuring the mechanical properties of individual NW. (b) Both ends of a NW fixed on the substrate over a deep trench. The scale bar is 500 nm. (c) A deformed Au NW. The scale bar is 1 μm. [87]

There is another widely used in-situ measurement method named three-point nano-indentation, shown in Figure 12 (a). The in-situ device involves an AFM cantilever equipped with a photodiode used for recording applied force. Similar to the aforementioned in-situ tensile testing device [84], [85], both ends of the specimen are fixed on a substrate by electron-beam-induced Pt wire, shown in Figure 12 (b), following the method proposed by Koops et al. [88]. The trench under the NW is created by focused-ion-beam milling with 0.3~4 μm in width and 250~500 nm in depth. The AFM cantilever is aligned parallel to the NW and force is applied perpendicular to the NW axis. During the experiments, force-displacement (F-d) data can be recorded to obtain the F-d curves. Combining the F-d curves and calculation equations which can be found in literature, the yield strength and Young's modulus of the examined MNWs can be obtained.

#### 2.2.2.2 Simulations of MNWs

Although various experimental methods have been developed, it is still a great challenge to characterize the mechanical properties of MNWs for a few reasons. First, it is challenging to fabricate free-standing MNWs due to the complex synthesizing processes. Second, some techniques are challenging to operate, such as SEM and TEM, and the accuracy of the experiment results needs to be concerned. Moreover, such experiments are costly and time consuming, and it is impossible to observe the evolution of mechanical behavior details during the experiments.

To overcome the limitations of experimental measurements and look deep into the deformation evolution details of MNWs, a large number of studies have been performed by Molecular Dynamics (MD) simulations, especially the uniaxial tensile measurements on MNWs. One of the most widely used software package for MD simulations is the Large-scale Atomic/Molecular Massively Parallel Simulator (LAMMPS) [89], which is an open-source simulation tool developed by Sandia National Laboratories. It is very convenient for researchers to use MD simulations to investigate mechanical behaviors of MNWs with different conditions by just modifying the parameters of the models and codes, such as size of the NWs, strain rate and temperature. Compared to experiments, it is easier to control the load conditions by some thermostats and barostats.

Size effect is an interesting phenomenon for nanomaterials. Many studies have been done to probe the mechanisms of size effect on MNWs through MD simulations [90]–[92]. Deng and Sansoz [90] investigated the twinning boundaries and free surface effects on gold NWs, and revealed that both the nano-twin density and NW diameter can affect the dislocation motion during tensile loading. Without free surface, it was reported that twinning space would not affect the yield strength of the gold NWs. When there is free surface, Shockley partial dislocations will escape to the intersection plane of the twin boundary and free surface. They proposed an equation to describe the conjunction effects of both NW diameter and twinning space on the critical resolved shear stress. Narayanan et al. [91] reported that strain-hardening effect in the five-fold twinned silver NWs was dependent on the diameter of the NWs, which is smaller in size would result in higher hardening effect and ductility. For MNWs, strain rate and temperature may affect the yield strength as well. MD simulations reveal that high strain rates will induce amorphization in MNWs, which may affect the plastic deformation modes in fcc MNWs [93]–[95]. Recently, similar high strain rate-induced amorphous transformation also has been found existing in hexagonal-close-packed (hcp) Ti NWs [96], but no deformation modes transition has been reported in hcp Zr NWs by Guder and Sengul [92].

However, there are some limitations for MD simulations as well, such as too fast strain rates and controversial accuracy. But MD method does have a lot of advantages compared to experimental methods in characterizing nanomaterials. It is becoming more and more important in today’s nanomaterial studies.

### 2.2.3 Deformation mechanisms of MNWs

In the past two decades, MD simulations have been widely used to investigate the mechanical properties of MNWs due to the advantages of MD method described previously. Therein, researchers expressed an extensive interest in elastic and plastic deformation mechanisms under different loading conditions. In this section, deformation mechanisms will be reviewed to understand the underlying criteria of deforming a single free standing MNW in different structural categories of fcc, bcc, and hcp.

#### 2.2.3.1 Deformation mechanisms of fcc MNWs

The deformation mechanisms of fcc MNWs have been extensively studied by researchers via MD simulations in recent years. The elastic deformation of fcc MNWs is generally understood by the homogeneous elongation of lattice unit cell along with the direction of loading [95]. Whereas, the plastic deformation varies with different loading types, strain rates, and intrinsic properties of the MNWs, which intrigues the strong interests of researchers. To date, two distinctive deformation mechanisms have been reported to mediate the structure evolution of fcc MNWs under loading: lattice reorientation and phase transformation.

Zimmerman et al. [97] reported that the plastic deformation of fcc MNWs was a combined effect of the intrinsic properties, loading type and orientation of axis, and free surfaces. They examined <100>- and <110>-oriented fcc MNWs and several different free surface packing modes with square cross-section. They found tension and compression could cause slipping with {110} side surfaces, while the closest packed {111} surface exhibited to inhibit the occurrence of slipping, thus deforming by twinning. The twinning phenomenon for <110>/{111}

MNWs can be attributed to the closest surface packing mode with the lowest surface energy. For <100>-oriented MNWs, both {100} and {110} side surfaces tend to cause twin boundaries under compressive loading, while NWs with {100} side surfaces will deform by slipping.

In recent years, complementary MD simulations have been performed to investigate the orientation and loading type effects on the deformation mechanisms of Cu NWs [98]. The compression-induced twinning deformation has been extended from <100>- to <103>- and <113>-oriented NWs. However, special twin-twin interactions have been observed only in <100>-oriented NWs. Under tensile loading, full reorientation occurs in <101>-, <103>-, <212>- and <214>-oriented NWs by twinning mechanism. But twinning in <100>-, <102>-, <111>-, <112>, and <113>-oriented NWs does not induce complete reorientation.

Based on previous studies, Kim et al. [99] believe that there is a competition between slipping and twinning mechanisms in fcc MNWs. They developed a Q-factor, which is described as the difference between activate energies of a second slip and trailing dislocation, to quantify the tendency of slipping and twinning. The misfit stress, elastic stress, and loading direction are incorporated in the Q-factor to determine the deformation mechanism, which has been validated by both experiments and MD simulations. Yin et al. [100] investigated the same competition behavior between slipping and twinning by experiments and MD simulations and found that the cross-section shape could affect the dislocation mechanisms as well. The results show that a higher aspect ratio of cross-section can cause the transition of deformation modes from twinning to slipping due to the variation of surface energies mediated by the cross-sectional shape.

Apart from the slipping and twinning mechanisms, a novel phase transition mechanism has been reported to be induced by a high strain rates [93]–[95]. Ikeda et al. [93] found that there was a critical strain rate (0.05 $ps^{-1}$) for pure Ni and CuNi NWs. A higher strain rate than the critical value would cause amorphization due to the reduction of melting point induced by high strain rate. However, no phase transformation could be observed with a lower strain rate and the NWs were deformed by dislocation motion. Similar phase transition in Au [101] and Ni [95] NWs has been reported, but with different critical strain rates. The amorphized NWs exhibit superelasticity characteristics under uniaxial loading and low-temperature conditions [94]. In 2015, a new and more complex strain rate-induced fcc-bcc-hcp (FBH) phase transformation mechanism for Cu NWs has been reported by Xie et al. [102]. At high strain rate ($4 \times 10^{10}$ $s^{-1}$) and low temperature (10 K), the novel FBH phase transition controls the plastic deformation. Without changing the temperature, lowering the strain rate can cause dislocation nucleation dominates the plastic deformation again.

#### 2.2.3.2 Deformation mechanisms of bcc MNWs

It is reported that bcc MNWs are preferred in various applications, such as shape memory and energy storage, compared to fcc ones [103]. Thus, bcc MNWs have attracted massive interest due to the outstanding mechanical behaviors. In this sub-section, the deformation mechanisms of bcc MNWs will be reviewed based on recent work, especially MD simulations. Similar to fcc MNWs, there are two main deformation mechanisms which are slipping and twinning [103]–[105]. Other mechanisms, such as phase transformation [106], [107], could occur under proper size, orientation, and strain rate conditions.

Wang et al. [103] investigated the deformation mechanisms of bcc Mo NWs by MD simulations. They find that slipping is expected to happen under uniaxial tensile loading in <110>- and <111>-oriented Mo NWs for lower surface energy, while twinning will dominate the plastic deformation in <100>-oriented NWs. Sainath and Choudhary [104] studied the coupling effects of size and temperature in ultrathin bcc iron NWs. Their results indicate that <100>-oriented NWs with smaller sizes and at high temperatures prefer to be deformed by slipping mode, while it is probably deformed by twinning mode at low temperatures and large sizes. They demonstrate the transition from slipping to twinning by a map, shown in Figure 13, under different sizes and temperatures. There is an obvious boundary separating the two regions where slipping mechanism dominates at the left with lower sizes but higher temperatures.

This figure has been removed for copyright issue.

**Figure 13.** The deformation mechanism map shows the preference of slipping and twinning in <100>-oriented bcc Fe NWs under different sizes and temperatures. [104]

To understand the competition between two types of twinning mechanisms in bcc MNWs, Shi and Singh [108] performed MD simulations on niobium, iron, tantalum, molybdenum, and tungsten NWs with <110>/{111}, <100>/{110}, and <100>/{100} orientations where <XXX> indicates the loading direction and {YYY} represents the side surfaces. Two distinctive twinning mechanisms have been observed: one, reflection twinning, is caused by the glide of 1/6<111> dislocations nucleated from the surface; the other one, isosceles twinning, is induced by the dissociation of the 1/6<111> dislocation into two partials of 1/12<111> gliding on adjacent {112} planes. The transition of two kinds of twins is reported to be mediated by the stable twinning fault energy $\gamma^{stf}$. The calculations reveal that Ta, Nb, and Fe favor the isosceles twinning mechanism, while Mo and W prefer coherent twinning.

This figure has been removed for copyright issue.

**Figure 14.** (a) Schematics of two twin boundary (TB) structures. (b) The dissociation of 1/6<111> dislocation on {112} planes. (c) Formation of asymmetric isosceles TB structures. [108]

Phase transformation also can be observed in bcc MNWs under uniaxial tension. Xie et al. [107] investigated strain rate and temperature effects on the deformation mechanisms in bcc iron <110>-oriented NWs. They developed a deformation mechanism map with respect to different strain rates and temperatures, shown in Figure 15, to illustrate the variation of mechanisms with different conditions. The map indicates that dislocation nucleation dominates the plastic deformation at low strain rate and high temperature, while bcc-to-hcp martensitic transformation occurs at high strain rate and low temperature. The phase transition is induced by the low energy barrier at high strain rate and low temperature.

This figure has been removed for copyright issue.

**Figure 15.** Plastic deformation map indicates the temperature and strain dependence in bcc iron NWs. [107]

### 2.2.3.3 Deformation mechanisms of hcp MNWs

In recent years, hcp MNWs also have drawn a lot of attention from researchers due to the superconducting [109] and magnetic [110], [111] properties. The high strength and low-density property make Ti a potential material for nanoelectronics and biomedical techniques. Thus, it is very important to understand the deformation mechanisms of Ti NWs under uniaxial loading. Like other structural MNWs, strain rate and NW size also can affect the mechanical behavior of hcp Ti NWs. MD simulations reveal that the twinning mechanism causes the initial yielding behavior for Ti NWs with different sizes under each strain rate [112], [113]. However, after saturation of twinning volume fraction, post-plastic deformation mechanisms dramatically depend on the strain rate and wire size [112]. Phase transformation from hcp to fcc favors happening at low strain rate $10^8 \sim 10^9$ $s^{-1}$. But size dependence becomes dramatic at a higher strain rate, > $10^9$ $s^{-1}$, and the deformation mechanism changes from phase transition to prismatic dislocation. A higher strain rate may transform the single crystalline NW to polycrystalline counterparts, shown as Figure 16. After that, both grain boundary motion and dislocation motion can be observed depending on the wire size.

This figure has been removed for copyright issue.

**Figure 16**. Size and strain rate effects on plastic deformation mechanisms in Ti NWs. [112]

Another work done by Chang et al. [96] reveals that $[11\bar{2}1]$-oriented Ti NWs are insensitive to the variation of strain rate, but with complex initial yielding behaviors with the combination of nucleation of several partial dislocations and twins. The transformation between deformation faults and twins can be observed for further plastic deformation. For

$[\bar{1}100]$-oriented Ti NWs, dislocation slip dominates the plastic deformation at all strain rates. Twinning faults dominate the deformation mechanism in [0001]-oriented Ti NWs.

In summary, the deformation mechanism is a complex function of both intrinsic properties and extrinsic conditions. There are three dominant deformation mechanisms in all structured MNWs, which are dislocation slipping, twinning, and phase transformation. Different mechanisms can be transformed by altering the size of the NWs, cross-sectional shape, temperature, strain rate, and loading orientations. Previous work is very important to help researchers to understand mechanical behaviors and design novel MNWs.

## 2.3 Alloying effects on the mechanical properties of metals

Nowadays, obtaining metal products with optimal properties has become one of the most important tasks of modern physical metallurgy. Alloying has been reported as one of the most effective methods to achieve this goal. For nanocrystalline metals, it is reported that alloy can be used to improve thermal and chemical stability and hinder grain growth behavior [114]. Moreover, solute atoms can dramatically affect the mechanical performance of the metals, which guarantees the wide usage of alloys. With additional solute atoms in the metal matrix, the yield strength is expected to be improved, which is widely known as solid solution strengthening or solid solution hardening (SSH) effect [13]. Nevertheless, the existence of solute atoms may also lead to the opposite phenomenon, which is lowering the strength of the alloys, and described as the solid solution softening (SSS) effect [115]. Those two primary alloying effects have been comprehensively investigated during the past decades. In this section, both will be reviewed based on recent work.

### 2.3.1 Solid solution strengthening effects

Traditionally, alloying is used to enhance the strength of metals, which has been extensively adopted by engineers in the long history of physical metallurgy. There are two primary models describing the SSH effect, which are strong-pinning model [116], [117] and weak-pinning model [118], [119]. The former considers the effect of a single solute atom, which serves as a pin to hinder the dislocation motion. While the latter concerns the collective effects of randomly distributed solute atoms interacting with dislocations. Thus, fluctuation of the dislocation pathway reduces the dislocation energy, and those dislocation bows out of the pinned regions, resulting in additional stress, and inducing higher yield strength. In recent years, the phenomena, and underlying mechanisms of SSH become one of the most popular topics in nano-material science, especially with the emergence of medium entropy alloys (MEAs) and high entropy alloys (HEAs).

For polycrystalline pure metals, it is reported that grain growth at room temperature [120] or under stress [121] may occur when the grain size comes to nano-scale. However, it has been found that can be used to enhance the stability of grain structures and hinder the grain coarsening behavior by the pinning effect of grain boundaries stabilized by solute atoms [122]. In other words, it also can be considered as an indirect SSH effect caused by solute atoms. A direct SSH phenomenon has been reported by MD simulations of additional Ni atoms in Cu matrix [123], which can be attributed to the increase in Young's modulus caused by additional Ni atoms. Zhang et al. [124] investigated the SSH effect in Ni-based superalloys, in which Re, Ru, and Co serve as the solute atoms. All three kinds of elements at high concentrations can significantly strengthen the superalloy which can be attributed to the pinning effect of the solute atoms randomly located in the slipping planes.

In recent years, massive work has been done to investigate the SSH phenomenon and underlying mechanisms in HEAs and MEAs. For the famous Cantor alloy FeCoNiCrMn [125], it is reported that the addition of Al (0~20 at.%) will cause phase transition from the initial fcc single phase to duplex phases, and finally to bcc single phase [126]. In the mixed phase region, the yield strength is obviously increased but with ductility reduced. Based on previous work, Kumar et al. [127] investigated the SSH effect of addition of Al ranging from 0.25 to 5 at.% in the Cantor alloy matrix. Both experimental and Density Functional Theory (DFT) simulation results indicate that the addition of Al causes dramatic lattice distortion compared to the Cantor alloys without Al atoms [128], [129]. According to the mechanical characterization of the samples, higher Al concentration results in higher yield strength and ultimate strength, which can be attributed to the increase in local lattice distortion.

Recently, novel refractory high entropy alloys (RHEAs) HfNbTaTiV and TiNbTaZrHf, etc., and refractory medium entropy alloys (RMEAs) NbTaTi and WNbTaTi, etc., have become hot topics among the studies of HEAs and MEAs due to the remarkable high-temperature resistance [130]–[132]. The atomic-size mismatch in RHEAs [133] is considered to be larger than in Cantor alloys [128], [129], which is expected to cause considerable lattice distortions in the matrix. Nevertheless, the lattice distortion is closely related to the structural stability and mechanical properties of the HEAs [127], [130]. Thus, the lattice distortion induced SSH effects in RHEAs have been extensively studied by both experiments and theoretical calculations.

The lattice distortion in RHEAs is significant due to the atomic size misfit, shown in Figure 17, which induces the dislocation propagation more difficult compared to pure metals [130]. Thus, the consequence of severe lattice distortion is enhanced mechanical properties. By using the maximum lattice distortion principle, a novel RHEA (HfNbTaTiV) has been developed by Han's group [134]. The newly developed RHEA is reported to be able to retain 53% of the room temperature yield strength under 700 °C, which is much more outstanding than other RHEAs. Their work sheds new light on designing novel alloys for future physical metallurgy development.

This figure has been removed for copyright issue.

**Figure 17.** Schematic illustration of lattice distortion in a BCC structural RHEA. (a) Perfect lattice of Ti. (b) Slightly distorted lattice caused by additional Nb. (c) Significantly distorted lattice of the RHEA. [130]

### 2.3.2 Solid solution softening effects

In contrast to the strengthening effect, solute atoms may serve as a weakening trigger to the mechanical properties of metals, which is defined as SSS effect. The SSS phenomenon was first reported for exploring the solid solution effects on body-centered cubic (BCC) metals in 1960s. The theoretical calculation results of activation parameters were found consistent with the experimental values, and reduction in Peierls' stress with the addition of solute atoms inducing the softening effect on the strength [115], [135].

For BCC Mo-based binary alloys, the SSS effect is reported to have an intrinsic nature.

The addition of elements with excess electrons, for instance Pt, Ir, Os or Re as the solute atoms, the impurity electron structures are deemed to take the responsibilities of changing in local chemical bonding, reduction of generalized stacking fault energies (GSFEs) and shear resistance in atomic scale, which intrinsically facilitates the double kink nucleation and enhances the dislocation motion [136]–[138]. In contrast, the addition of Hf or Ta atoms into the Mo lattice will cause the hardening effect, due to the lack of electrons in the outer shell.

For the equal atomic face-centered cubic (FCC) alloy CoCrFeMnNi, known as the Cantor alloy, the minor addition of Al atoms will induce the reduction of Peierl's stress, resulting in softening in hardness [139]. The SSS effect was also found in single crystal Ni-Co alloy nanoparticles both experimentally and theoretically by Bisht et al. [140], which is in contrast to the strengthening effect induced by the addition of Co atoms into Ni-based superalloys [124]. Interestingly, the strength-composition profile reveals that there is a minimum strength value when the atomic fraction of Co is around 0.15, then, the higher yield strength is expected with higher Co concentration, albeit lower in strength than the pure Ni nanoparticle. This extraordinary softening phenomenon can be explained by the competition between the reduction of dislocation nucleation and the pinning effect caused by the existence of solute atoms.

However, the solute effects may not always be monotonic. The transition between strengthening and softening effects may happen in some scenarios, like the shifting behaviors due to the variation of Co fractions in defect-free Ni-based nanoparticles [140]. Similarly, the transition from softening to strengthening occurs in tungsten-based alloys [141]. Small fractions of solute atoms in the VI, VII, and VIII groups added into BCC tungsten are reported to lower the critical resolved shear stress (CRSS) by enhancing the nucleation of double kinks. After the critical solute concentration, the higher concentrations of solute atoms will result in higher CRSS values, when the solute pinning mechanism comes to dominate the dislocation mobility. Differently, the first strengthening followed by softening behaviors was unveiled in Fe-Ni alloy NWs at 1 K, which can be attributed to the transition of deformation mechanisms from the twinning to dislocation slip owing to the addition of more Ni atoms [142]. However, a linear softening effect by increasing the Ni concentration was found at 300 K, where dislocation motion dominated the deformation mechanism.

Although the strength is reduced, the flip side of the coin is that the SSS may improve the ductility and toughness of the alloys. For instance, with the addition of Co atoms into the defect-free Ni nanoparticles, the toughness is monotonically increased, which can be explained by the pinning effect of the solute atoms [140]. Adding minor fraction of aluminum solutes into the Cantor alloy will soften the material, but the ductility can be enhanced [139]. Similar phenomena were also reported in bcc tungsten-based alloys [141] and fcc silver-based alloys[143]. To improve the ductility of hcp Mg-based alloys, Tsuru et al. [144] employ the SSS strategy to find out that yttrium (Y) is a potential solute element by the significant reduction of generalized stacking fault energy (GSFE). Thus, to obtain better ductility, the SSS method may be a competitive way to design new alloys while compromising the softening in strength.

# Chapter III Computational methodology

## 3.1 MD simulation tools

MD simulation is a powerful technique for computing the thermodynamic, chemical, and mechanical properties of a classical many-body system [145], which means the particle motion in the system is set to obey the classical mechanics. There is no need to worry about the quantum effect except for translational or rotational motions of light atoms or molecules, or vibrational motion with $h\nu > \kappa_B T$, where h is the Planck constant, $\nu$ is the frequency of vibration behavior, $\kappa_B$ is the Boltzmann constant, and T is the temperature of the particle.

Similar to real experiments, MD simulations undergo some procedures, such as model preparation, measurement of properties, and analysis of the results. In this project, all the MNW models are constructed by the open-source program named Atomsk [146], which can be used to manipulate and convert atomic configuration files. Another open-source software package named OVITO [147] has been employed for 3D visualization of the model configurations. The common neighbor analysis (CNA) method [148] is used to perform structure identification, which is based on the decomposition of the radial distribution function (RDF) according to the local environment of atomic pairs. Dislocations are identified and analyzed by the dislocation extraction algorithm (DXA) [149], which is combined in the OVITO package. In this project, all the atomistic simulations are implemented by using the open-source software package LAMMPS [89], which is initially developed by the Sandia National Laboratories and its partners. It is a particle-based powerful modeling of various materials and widely used tool.

## 3.2 Uniaxial tension of MNWs with randomly distributed solutes

### 3.2.1 Ni-based binary alloy NWs

The simulations start from Ni-based alloy systems, since they exhibit outstanding mechanical and electrochemical properties, and attract dramatic interest from researchers. Moreover, Ni-based alloys have been widely used in temperature and corrosion resistance applications [35], [150]–[152]. Thus, it is quite essential to understand the alloying behavior in Ni-based alloys, which will help to design novel Ni-based alloys in turn.

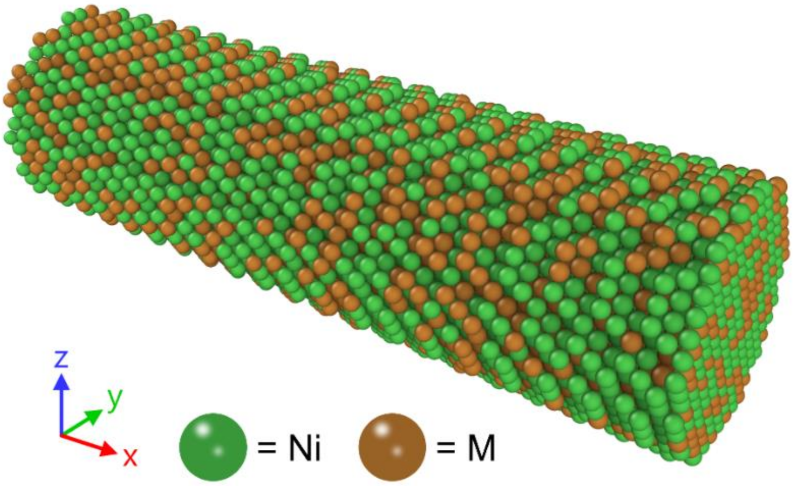

**Figure 18.** Schematic illustration of the cylindric Ni-based alloy MNW models with solute atoms M (M = Cu or Co). The axial dirextion of the MNW is parralel to the x-axis.

In this project, various Ni-M (M is Cu or Co) single crystalline binary alloy NWs have been constructed by Atomsk [146]. Solute atoms M are randomly distributed in the NWs by substitution of Ni atoms, shown in Figure 18, in which, the green spheres represent the host Ni atoms, while the brown ones indicate the solute atoms. In all cases, the axial directions of the MNWs are set parallel to the *x*-axis. To understand the orientation effects on the solute softening phenomenon, various axial directions of Ni-Cu NWs have been constructed along with $\langle 111\rangle$, $\langle 100\rangle$ and $\langle 110\rangle$, since they are expected to be plastically deformed with different mechanisms[97], [98]. For Ni-Co systems, all the MNWs are set to $\langle 111\rangle$-oriented. The diameter of all the Ni-based alloy NWs is ~4 nm, and the length-to-diameter ratio of each MNW is set to be ~3.3, which is similar to Refs. [77], [153].

Another critical variable for these models is the composition of the solute atoms in the alloy MNWs. According to the phase diagrams of the two alloy systems, the Ni-Cu is an isomorphous system with unlimited solubility at high temperatures [154], and so does the Ni-Co system [155]. It is reasonable to investigate the two alloy systems in an abroad solute concentration range without worrying about the appearance of a secondary phase. The concentration of Cu ranges from 0 to 100 at.%, while the content of Co in the Ni-Co system is chosen from 1 to 60 at.% for comparison with Ref. [140]. Simplified labels are used to represent Ni-M MNWs: Ni-M$x$-$\langle uvw\rangle$ is used for representing the Ni-M NWs, in which, $x$ refers to the atomic fraction of the nominal solute atoms, and $\langle uvw\rangle$ refers to the orientation of the NW axis.

As for the interatomic force field, the embedded-atom method (EAM) potential developed by Onat and Durukanoğlu [156] has been used to evaluate the interactions of Ni and Cu binary alloy system, which was determined by fitting both experimental and first-principle data of Ni-Cu system. For comparison of the effects of different potentials, three kinds of potentials have been employed for Ni-Co NWs: the Ni-Co system EAM potential developed by Mishin et al. [157] which has been used in Ref. [140]; the HEA system (CoCrCuFeNi) EAM potential developed by Deluigi et al. [158]; and the second-nearest-neighbor modified embedded-atom method (2NN MEAM) potential for binary Ni-Co system developed by Kim et al. [159].

The MD simulations are then performed for each model by using the open-source software package LAMMPS [89] with a constant timestep (1 fs) throughout the whole simulation process. Periodic boundary condition is set to the MNW axial direction, while leaving the other directions as free surfaces. To relax the MNW structure, the constant-volume, constant energy ensemble (NVE) is firstly applied at room temperature (300 K) for a duration of 50 ps, followed by another relaxation at the same temperature by using the isothermal-isobaric (NPT) ensemble at zero pressure in the axial direction for another 50 ps. Thus, each MNW model can be sufficiently relaxed before uniaxial deformation is applied.

After the relaxation, the uniaxial tension is performed for each MNW with a constant strain rate ($10^9$ $s^{-1}$), combined with the canonical ensemble (NVT) at room temperature. The average atomic stresses in axial direction are calculated using the virial theorem [160]. Snap shots are taken during the tension process for post observation and analysis by OVITO [147].

### 3.2.2 Cu-Ag alloy NWs

The immiscible alloy system Cu-Ag has also been investigated to search for the softening phenomenon. Two types of models, Ag-Cu$x$ and Cu-Ag$y$ NWs have been created by Atomsk with similar size to the Ni-based alloy NWs and oriented with ⟨111⟩ direction. Solute atoms (Cu or Ag) are randomly distributed in the NW models with the concentration ranging from 1 to 10 at.%. The EAM potential developed by Mishin et al. [161] is used to represent the interatomic interactions of the alloy system. All the other simulation details are the same as the Ni-Cu system, which has been described previously.

### 3.2.3 Complex alloy systems

To investigate the softening phenomenon in complex alloy systems, an MEA alloy system CuFeNi and the corresponding HEA alloy system CoCrCuFeNi have been employed to perform uniaxial tensile testing. Copper is chosen as the solute in both alloy systems, with the concentration ranging from 12 to 48 at.%. The MNW model is shown in Figure 19. All the MEA and HEA NW axes are set to ⟨111⟩-oriented and created by random substitution method.

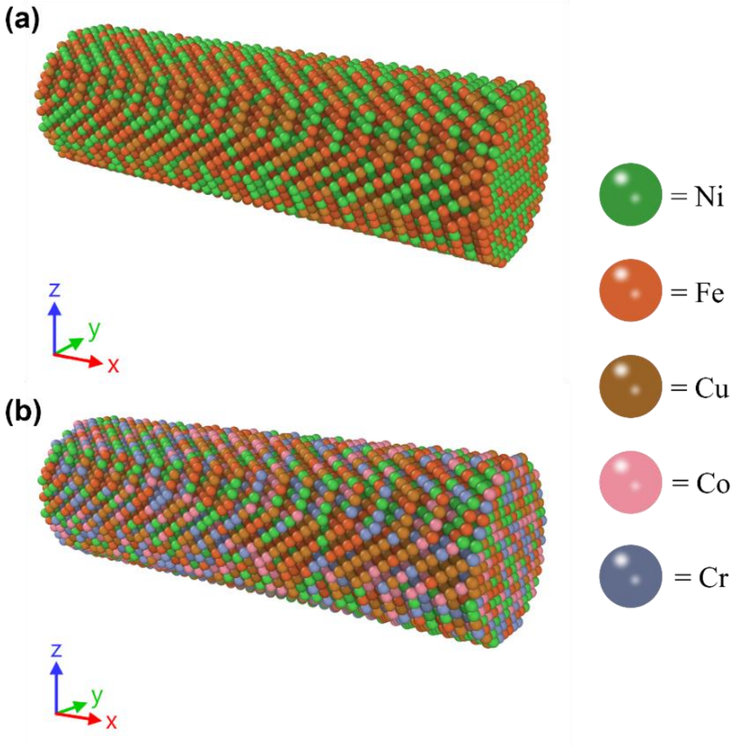

**Figure 19.** Illustration of the MEA NW and HEA NW models, in which each element is randomly distributed in the NW model. (a) $(NiFe)_{100-x}Cu_x$ ⟨111⟩-oriented NW model, atoms are randomly distributed in the NWs. (b) $(CoCrNiFe)_{100-y}Cu_y$ ⟨111⟩-oriented NW model.

Each model is then tested by uniaxial tensile MD simulations with the same processes and conditions described in previous Ni-based alloy NW uniaxial tension. The EAM potential developed by Deluigi et al. [158] has been employed to evaluate the interatomic interactions for both MEA and HEA alloy NWs.

### 3.2.4 Generalized planar fault energy calculation

In fcc MNWs, it is probably plastically deformed by slipping or twinning mechanisms which depend on the orientation and loading type [97]. The slipping is formed by the nucleation and propagation of the $\frac{1}{6}\langle 112\rangle$ partial dislocations on the closest packed {111} planes. To form twin boundaries, the $\frac{1}{6}\langle 112\rangle$ partial dislocations need to nucleate and propagate on the adjacent {111} planes [97]. Thus, the energy barriers of these two types of planar faults are believed to control the deformation and failure of MNWs [162].

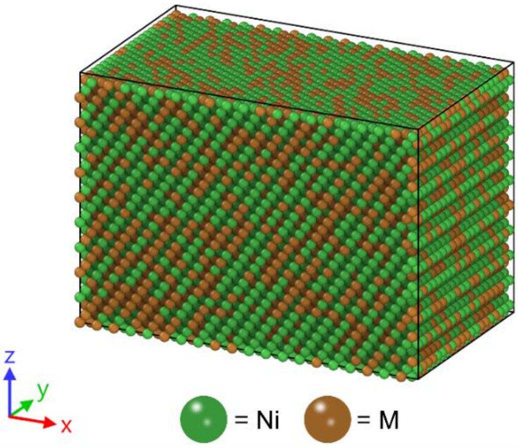

**Figure 20.** Illustration of the supercell for Ni-based alloy systems. The atomic sites are randomly occupied by Ni and M.

To calculate the generalized planar fault energies, the method described in Refs. [163], [164] is followed. A rectangular supercell has been constructed with x, y and z axes oriented in $\langle 112\rangle$, $\langle 110\rangle$ and $\langle 111\rangle$ directions, respectively. The supercell contains 24000 atoms in total with a size of $86 \times 50 \times 61$ nm$^3$. For all alloy systems, the concentrations of solute atoms are the same as the corresponding uniaxial tension testing models. The atomic sites are randomly occupied by the corresponding solvent and solute atoms. Figure 20 shows an example of the supercell for Ni-based alloy systems, where the host atoms Ni and solutes M (M is Cu or Co) are randomly distributed in the supercell. Supercells for NiFe-Cu and CoCrNiFe-Cu systems are the same size and random distribution of each element.

Periodic boundary conditions are set to $\langle 112 \rangle$ and $\langle 110 \rangle$ directions and leave the $\langle 111 \rangle$ direction with free boundary condition. Each supercell is divided into top and bottom regions along with $\langle 111 \rangle$ direction, while each region contains half of the supercell. To form a stacking fault (SF), the bottom half is fixed, while the upper half is rigidly shifted in $\langle 112 \rangle$ direction by small increments step by step until the total displacement reaches the length of the Burgers vector of the partial dislocation $a_0/\sqrt{6}$ where $a_0$ is the lattice constant of the supercell. Similarly, to form a twinning fault (TF), the SF regime and lower layers are fixed, then rigidly shifting the rest layers along with $\langle 112 \rangle$ direction in $\{111\}$ plane by small increment until reaching displacement of $a_0/\sqrt{6}$. During the step-by-step shifting, the energy of each displacement is calculated by energy minimization with a conjugate gradient (CG) algorism. Then, the energies are used to calculate the corresponding stacking fault energy (SFE) and twinning fault energy (TFE).

## 3.3 Hybrid molecular dynamics/Monte Carlo simulations

### 3.3.1 Ni-based binary alloy NWs

To understand the influence of solute distribution on the softening effect in Ni-based binary alloy NWs, hybrid molecular dynamics/Monte Carlo (MD/MC) simulations have been performed and followed by similar uniaxial tensile testing to investigate the mechanical behaviors after hybrid MD/MC simulations. Initially, periodic boundary condition is used in all directions. The timestep is set to 1 fs. The structure of each MNW model is optimized by energy minimization using the CG algorithm. Then, each model is relaxed by using the NPT ensemble at 300 K under vacuum atmosphere for 50 ps. After the relaxation, hybrid MD/MC simulations are then implemented using the Metropolis algorism [165], with a smaller timestep 0.1 fs to keep the stability of the system. One atom swap is performed every 10 MD steps. The duration of hybrid MD/MC is 5 million steps in total to make sure the sufficiency of atomic exchanges. The resulted models of hybrid MD/MC simulations are then served as the input models for post uniaxial tension simulations, in which all conditions are the same as previously described in section 3.2.1.

### 3.3.2 The Cu-Ag alloy NWs

In recent years, the immiscible Cu-Ag alloy system attracts massive interest due to its outstanding conductivity [166], [167] and optical properties [168]. In this project, the Cu-Ag alloy NWs are also employed to investigate the influence of solute concentrations on the yield strength of the NWs. The NW model size is similar to Ni-based alloy NWs in section 3.2.1. All the Cu-Ag alloy NW axes are oriented in $\langle 111 \rangle$ direction. The concentration of solute atoms ranges from 1 to 10 at.% whenever Cu or Ag serves as the solute. Initially, the solute atoms are randomly distributed in each NW model. Due to the immiscibility of the Cu-Ag alloy system, hybrid MD/MC simulations are performed to investigate the alloying effect on the NW strength. The EAM potential developed by Williams et al. [161] has been employed to evaluate the interatomic interactions for the Cu-Ag alloy system. All other conditions are the same as described in section 3.3.1 except the duration of hybrid the MD/MC process, where 3 million timesteps are chosen since the lower concentration of solute atoms.

### 3.3.3 The Mg-Al alloy NWs

Another interesting binary alloy system Mg-Al has also been chosen to investigate the alloying effect on strength caused by the addition of Al into the Mg matrix. An hcp Mg NW is firstly created by using Atomsk [146]. Then, some of the host sites are randomly substituted by solute atoms (Al or Mg), whose concentration ranges from 2 to 12 at.%. Each NW model has a similar size to the aforementioned Ni-based NWs. The EAM potential developed by Mendelev et al. [169] for Mg-Al binary alloy system is employed to represent the interatomic interactions. All the simulation processes and other parameters are the same as described for Cu-Ag alloy NWs in section 3.3.2.

# Chapter IV Computational results and discussions

## 4.1 Results of MNWs with randomly distributed solutes

### 4.1.1 Results of Ni-based binary alloy NWs

The uniaxial tension stress-strain curves of Ni-Cu NWs with different compositions and orientations are shown in Figure 21, in which the maximum strain for ⟨111⟩- and ⟨110⟩-oriented NWs is 10%, shown in Figure 21 (a) and (c), respectively. While the maximum strain calculated for ⟨100⟩-oriented Ni-Cu NWs is set to 15%, shown in Figure 21 (d). Apparently, the yield point is easy to see and no strain hardening phenomenon can be observed in each Ni-Cu NW model. The yield strength of each alloyed Ni-Cu NW is lower than the value of pure Ni NW and higher than the yield strength of the pure Cu NW model, no matter what the orientation of the NWs is. For the alloyed Ni-Cu NWs, it can be found that the higher copper concentration will result in lower yield strength, and the trend is applicable to all three different orientations. This trend is different from the typical solute solution hardening effect in bulk Ni-Cu system where the strength of the alloy is higher than both pure Ni and Cu within a certain composition range, which is shown in Ref. [82].

The relationships between yield strength, Young's modulus, and the solute concentration with respect to the NWs of three different orientations are shown in Figure 22 (a) and (b), respectively. Both yield strength and Young's modulus are linearly reduced by increasing the copper concentration, which is applicable to all three orientations. The trend indicates that softening phenomenon is present in single crystalline Ni-Cu alloyed NWs, and higher copper concentrations will linearly soften both yield strength and Young's modulus. Moreover, the softening phenomenon is insensitive to NW orientations. However, a strengthening phenomenon can be obtained by reducing the copper concentration, which is quite special for the Ni-Cu alloy system, since the yield strength of the alloy NWs is linear to the solute composition and may not be observed in other alloy systems.

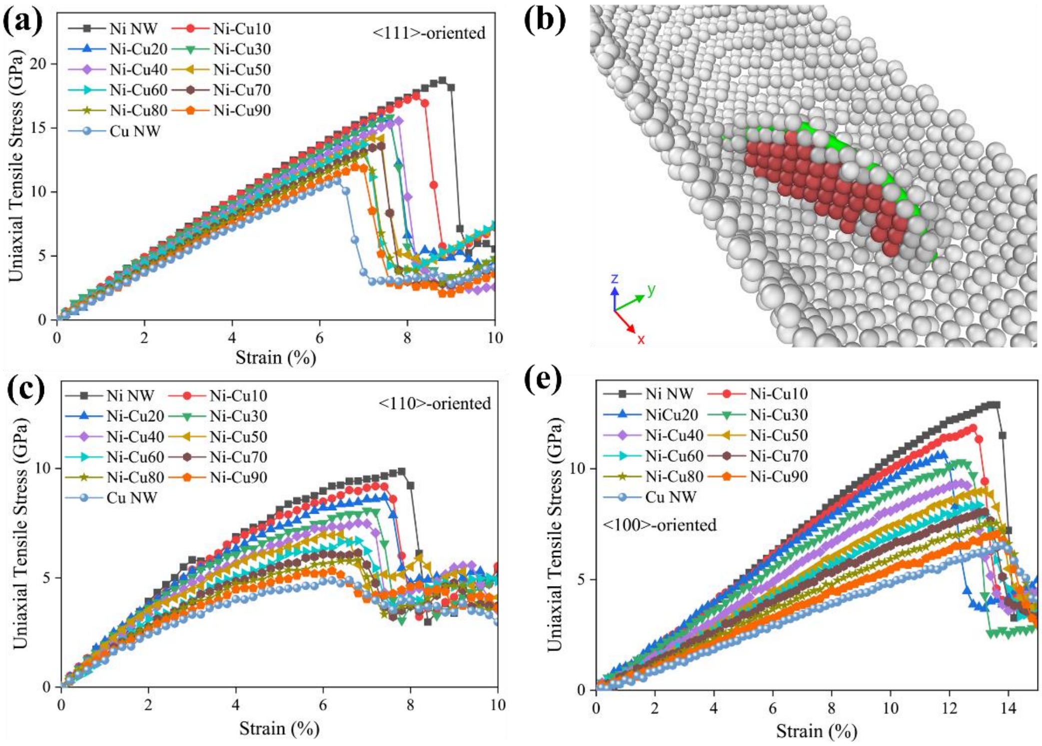

**Figure 21.** Uniaxial tensile stress-strain curves of Ni-Cu NWs with different concentrations and orientations (a) ⟨111⟩-oriented NWs, (c) ⟨110⟩-oriented NWs, and (d) ⟨100⟩-oriented NWs. (b) shows the nucleation of the first partial dislocation from the surface in the Ni-Cu*30*-⟨111⟩ NW, where red atoms represent SF, and the green line represents the partial dislocation. The diagrams illustrate that the Ni-Cu alloyed NWs are softened by increasing the Cu addition.

It is well known that Young's modulus is representative of the material's stiffness and resistance to elastic deformation [82]. The softening in Young's modulus will cause reduction in the stiffness of the material. Although the softening phenomenon can reduce the strength of the material, it may improve the ductility and toughness which has been proved by researchers [140]. In some cases, softening is very useful for improving ductility, such as the addition of

Re in W [141], [170], [171].

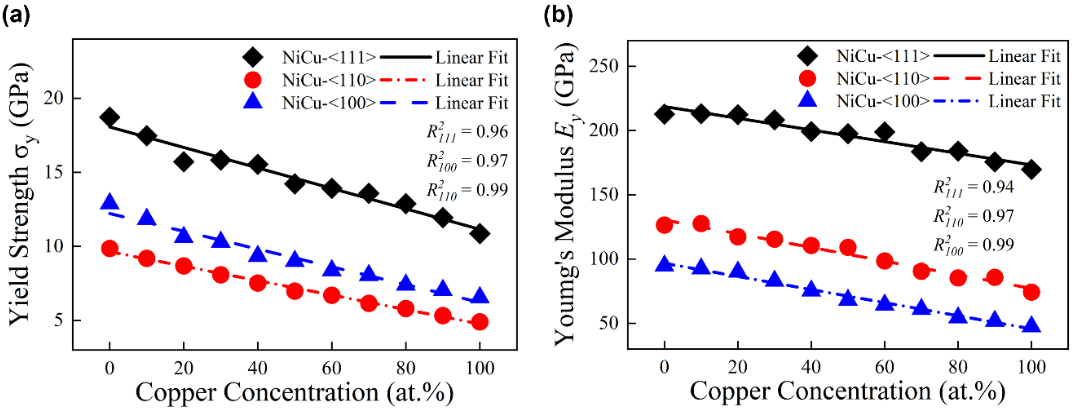

**Figure 22.** Comparison of the yield strength and Young's modulus of different oriented NWs against the copper concentration. (a) The yield strength $\sigma_y$ of different oriented NWs is linearly softened by increasing the copper addition. (b) The Young's modulus $E_y$ is also linearly softened by increasing the copper atoms, where the $E_y$ values are obtained by calculating the slope of the strain interval 0~4%.

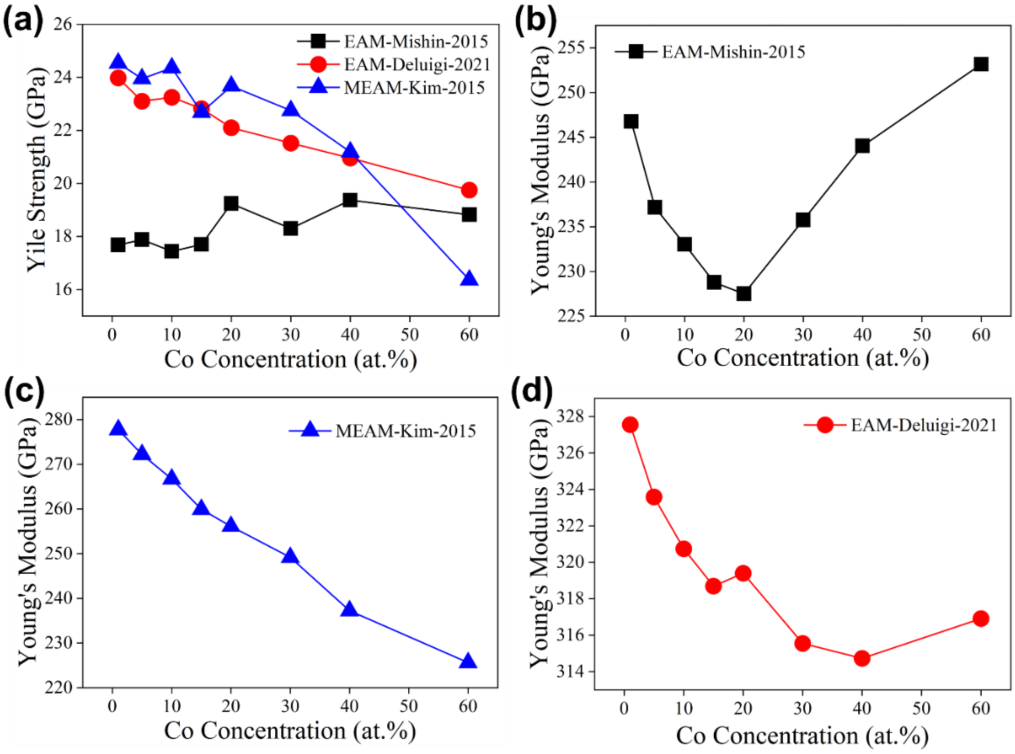

**Figure 23.** Uniaxial tension results of Ni-Co NWs, in which Co atoms are randomly distributed, under different interatomic potentials: (a) shows the yield strength of Ni-Co alloyed NWs versus different Co concentrations; (b), (c) and (d) illustrate the variation of Young's modulus under different Co concentrations. The Young's moduli are obtained by calculating the slope of the strain interval 0~4%.

To compare with the work that has been done by Bisht et al. [140], we performed MD simulations to investigate the softening effect of Ni-Co-⟨111⟩-oriented alloy NWs with randomly distributed solutes under different potentials. Similar to Ni-Cu-⟨111⟩-oriented NWs, each Ni-Co alloyed NW yields by nucleation of partial dislocations without strain hardening. The results are shown in Figure 23, where (a) shows the variation of yield strength under different interatomic potentials. Apparently, the trends of yield strength against Co concentration are significantly different from each other. Both results of the EAM-Deluigi and MEAM-Kim exhibit softening phenomena. However, the results of EAM-Mishin exhibit an initial slight fluctuation until the concentration of Co comes to about 15-at.% and followed by a slight strengthening phenomenon. This non-monotonic chemical dependence of yield strength is also different from the behavior found by Bisht et al. [140], where they reported that the yield stress was dramatically reduced by increasing the Co concentration to 15-at.% and followed by an obvious strengthening trend by continuously increasing Co concentration to 60-at.%. They argued that two competing effects were caused by the addition of solute atoms: the reduction effect on the nucleation of first dislocation which can be observed in the both EAM-Deluigi and MEAM-Kim conditions but not in EAM-Mishin condition; the solute-induced friction hindering the dislocation motion after the formation of first dislocation. In this work, once the first partial is formed, the NW model yields and no strain hardening can be observed, which means that the yield behavior of Ni-Co alloyed NWs are controlled by the nucleation barrier of the first partial dislocation. Thus, for EAM-Deluigi and MEAM-Kim conditions, the existence of Co atoms reduces the energy barrier of first dislocation, while enhancing the dislocation energy barrier under EAM-Mishin condition.

As for Young's modulus, the corresponding curves of Young's modulus with different solute concentrations indicate the dramatically different effects of different potentials even using the same NW models. The Young's modulus of EAM-Mishin condition is initially softened by increasing the Co concentration until the critical value 20-at.%, followed by a strengthening trend, which is consistent with the atomistic simulations done by Bisht et al. [140]. A similar transition from softening to strengthening in Young's modulus can also be observed under EAM-Deluigi condition, but with a different critical Co concentration 40-at.%. However, the Young's modulus is monotonously softened by continuously increasing the Co concentration.

### 4.1.2 Results of Cu-Ag alloy NWs

For the Cu-Ag alloy NWs, the yielding mechanism is the same as Ni-based NWs, which is partial dislocation nucleation. Moreover, no strain hardening can be observed, which means that the yield strength is the exact tensile strength for the alloyed NWs. The results for Cu-Ag alloy NWs with randomly distributed solute atoms are shown in Figure 24, where (a) shows that the yield strength of both cases has been softened by increasing the solute concentration, which is very interesting and unexpected. Each yield strength for case-Cu-Ag*y* is higher than case-Ag-Cu*x*, which is easy to understand that copper is much stronger than silver, especially for the 1 at.% solute concentration. However, by gradually increasing the solute concentration, the yield strength for case-Cu-Ag*y* drops severely faster than the counterpart case-Ag-Cu*x*. The two yield strength values are very close for two cases when the solute concentration comes to 10 at.%. This bidirectional softening phenomenon is absolutely different from the monotonous softening trend. The Young's modulus gradually drops from 173.80 to 160.82 GPa while increasing the Ag concentration in Cu-Ag*y* NWs. However, the slight increase of Young's modulus from 112.36 (Cu-1 at.%) to 115.34 GPa (Cu-3 at.%) can be observed and followed by a flat region until the Cu concentration comes to 8 at.%. Finally, the Young's modulus is enhanced to 119.91 GPa when the copper concentration is 10 at.%. Thus, the overall trend for Young's modulus in case-Ag-Cu*x* is strengthened.

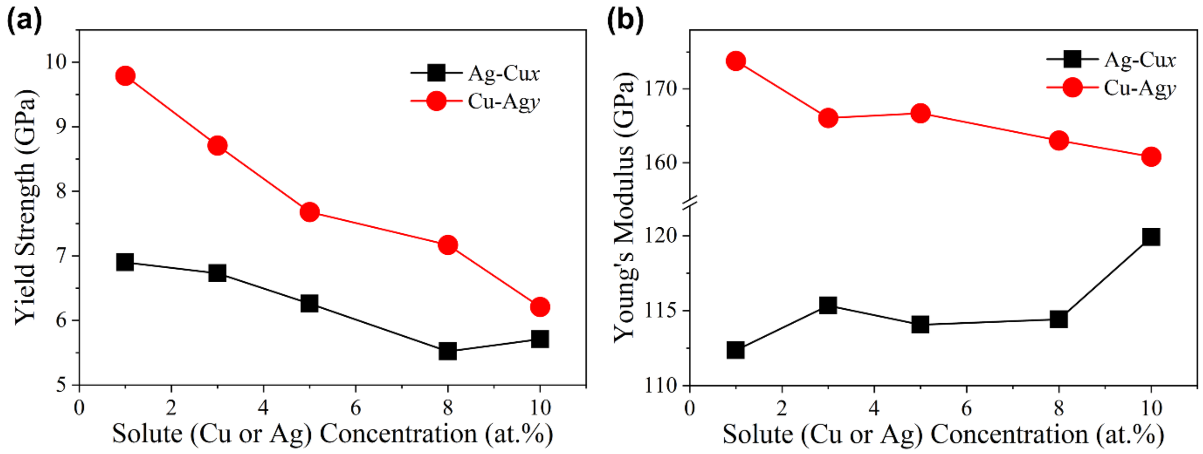

**Figure 24.** Uniaxial tension results for Ag-Cu alloy system: (a) shows the relationship between yield strength and solute concentration; (b) illustrates the relationship between Young's modulus and solute concentration. The Young's modulus values are obtained by calculating the slope of the strain interval 0~2%, which is different from the other alloyed NWs for the low yield strain.

### 4.1.3 Results of MEA and HEA NWs

To understand the chemical complexity effect on the softening phenomenon, the ⟨111⟩-oriented MEA (NiFe-Cu*x*) and HEA (CoCrNiFe-Cu*y*) NWs, in which solute atoms Cu are randomly distributed in each NW model, have been used to perform uniaxial tension simulations. Similar to the single crystalline Ni-based NWs, all these ⟨111⟩-oriented MEA and HEA NWs yield by the nucleation of the first partial dislocation and without strain hardening phenomenon, which can be observed from the stress-strain curves, shown in Figure 25 (a) and (b), respectively. By increasing the copper concentration, both the curve slopes and yield point are reduced.

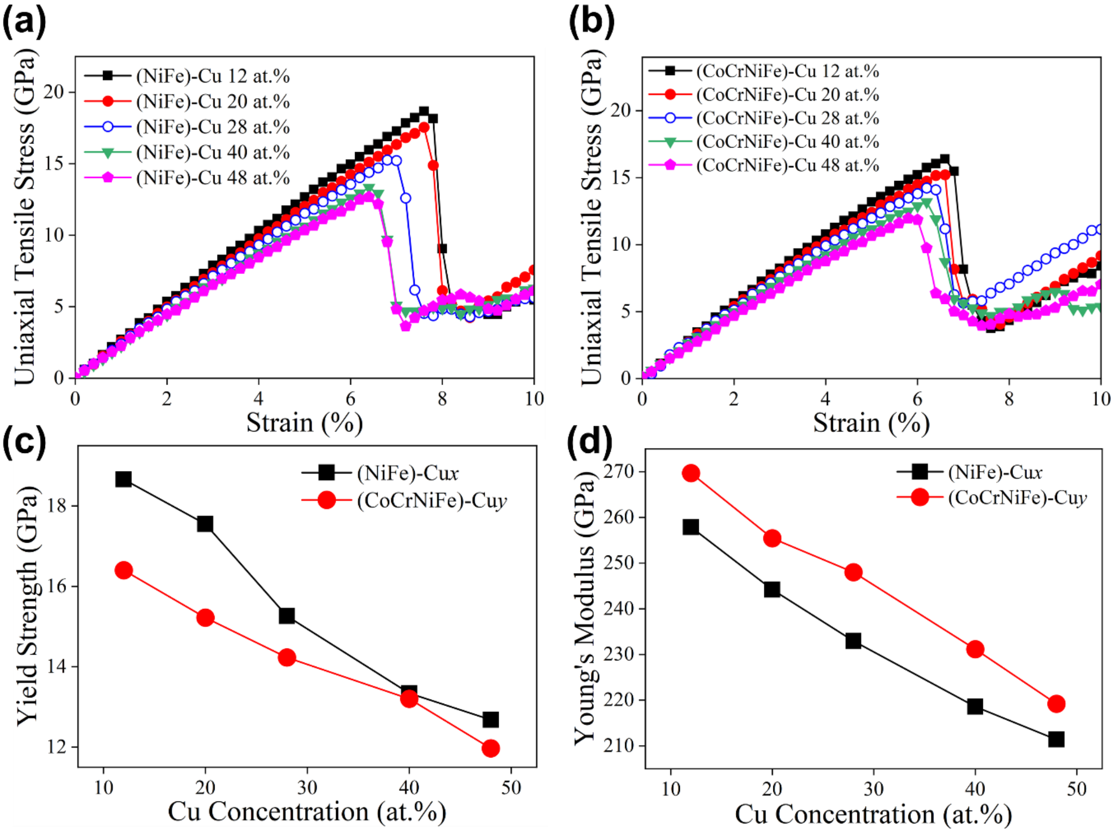

**Figure 25.** Results of uniaxial tensile simulations of solute randomly distributed MEA and HEA NWs: (a) and (b) represent the stress-strain curves of the MEA and HEA NWs, respectively; (c) comparison of yield strength versus copper concentration between the MEA and HEA NWs; (d) comparison of the composition dependence of Young's modulus between the MEA and HEA NWs.

The results of yield strength and Young's modulus against copper concentration are shown in Figure 25 (c) and (d), respectively. Apparently, both the yield strength and Young's modulus are monotonously softened by increasing the copper concentration in the MEA and HEA NWs. Moreover, the addition of Co and Cr can soften the NW in yield strength at the same copper composition (shown in Figure 25 (c)), while enhancing the Young's modulus (shown in Figure 25 (d)), which means that the existence of Co and Cr atoms makes the NWs stiffer but weaker. The phenomenon of softening the yield strength and strengthening the Young's modulus at the same Cu concentration is quite interesting and somewhat unexpected. The underlying mechanism will be discussed later.

### 4.1.4 Results of planar fault energy calculations

#### 4.1.4.1 Energy barriers for Ni-based alloy system

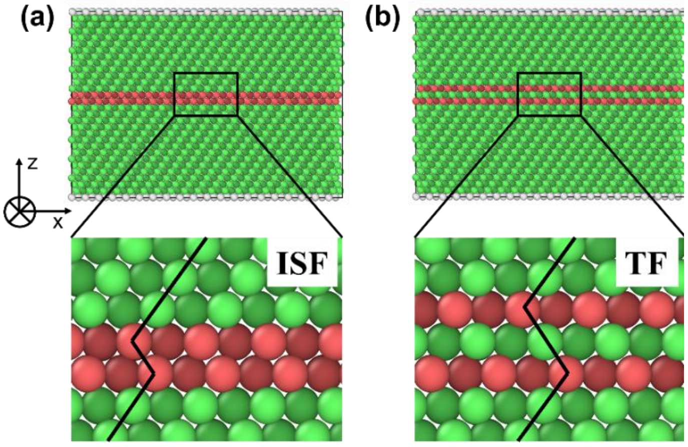

**Figure 26.** Illustration of the formation of an intrinsic stacking fault (a) and twinning fault (b).

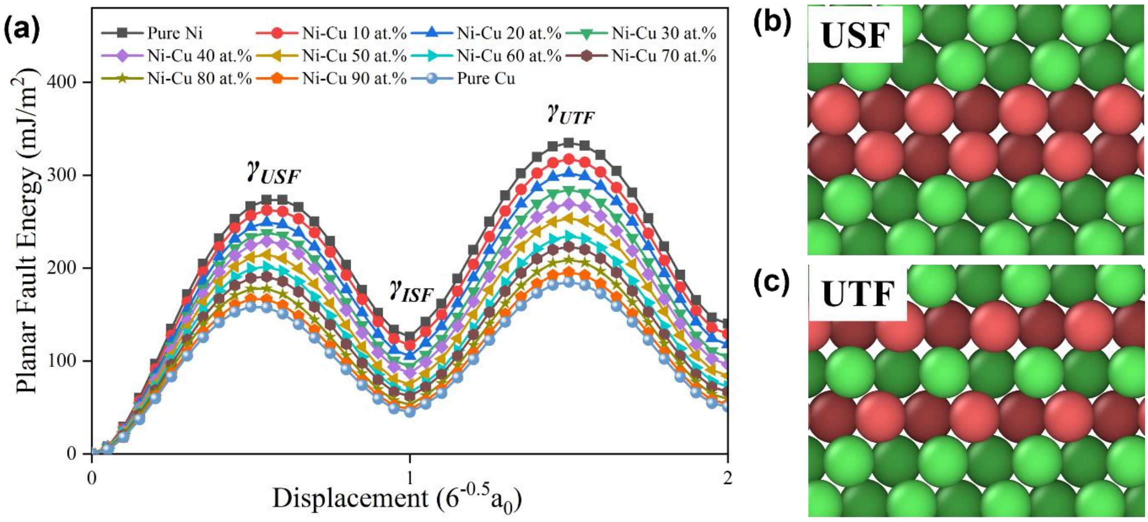

**Figure 27.** Results of planar fault energy calculation: (a) planar fault energy curves for Ni-Cu alloyed models, and pure Ni and Cu models; (b) and (c) illustrate the unstable stacking fault (USF) state and unstable twinning fault (UTF) state, respectively.

For the Ni-Cu alloy system, all the planar faulty energy for Ni-Cu alloy and pure Ni and Cu have been calculated via step-by-step displacement method, shown in Figure 26. It shows the formation of an intrinsic stacking fault (ISF) and twinning fault (TF), which both are formed by the slip along with ⟨112⟩ direction in the {111} planes. The difference is that the formation of a TF is caused by the either upper or lower layer slipping adjacent to the SF region. Thus, a stacking fault must be formed prior to the formation of a twin boundary by continuously slipping on adjacent {111} plane [97], which is the reason that the yielding mechanism is caused by the nucleation of the first partial dislocation in fcc metals.

The planar fault energy curves are shown in Figure 27 (a), where two peaks and a valley can be observed. The first peak is defined as the unstable stacking fault energy ($\gamma_{USF}$), which represents the unstable state during the formation of a SF, shown in Figure 27 (b). It is believed to be the energy barrier that controls the formation of a SF [162]. The valley of the curves is called the intrinsic stacking fault energy ($\gamma_{ISF}$), which indicates the energy difference of forming an intrinsic stacking fault (ISF). The second peak is defined as the unstable twinning fault energy ($\gamma_{UTF}$), shown in Figure 27 (c), which means the energy barrier for the formation of a twin. All the corresponding critical planar fault energy values for the Ni-Cu alloy system are listed in Table 1. According to the planar fault energy curves, all the values of $\gamma_{USF}$, $\gamma_{ISF}$ and $\gamma_{UTF}$ of pure Ni are much higher than pure Cu, which means the energy barriers of forming a SF and TF for pure Ni are much higher than pure Cu. And for each model, the $\gamma_{UTF}$ value is higher than $\gamma_{USF}$, which indicates that it is tougher to form a twin than a SF. Thus, the $\gamma_{UTF}$ values are considered as the controller of yielding behavior for Ni-based alloy NWs. Moreover, for Ni-Cu alloys, the energy barriers for both forming a SF and TF are monotonously reduced by increasing the copper concentration, indicating that higher copper concentration facilitates the formation of planar faults.

**Table 1.** Summarized energy barriers for SF, ISF, and TF in Ni-Cu alloy NWs. The 0 and 100 at.% Cu concentration refer to pure Ni and Cu cases, respectively.

| Cu Content, at.% | 0 | 10 | 20 | 30 | 40 | 50 | 60 | 70 | 80 | 90 | 100 |
|---|---|---|---|---|---|---|---|---|---|---|---|
| $\gamma_{USF}$, mJ/m$^2$ | 273.28 | 262.41 | 249.34 | 238.11 | 229.07 | 214.66 | 201.55 | 190.90 | 178.12 | 166.74 | 158.54 |
| $\gamma_{ISF}$, mJ/m$^2$ | 126.03 | 116.81 | 105.41 | 93.96 | 87.19 | 74.79 | 66.25 | 61.95 | 53.14 | 48.15 | 45.18 |
| $\gamma_{UTF}$, mJ/m$^2$ | 334.86 | 317.44 | 302.17 | 284.36 | 269.25 | 253.60 | 234.57 | 223.20 | 209.11 | 195.56 | 185.09 |

**Table 2.** Summarized energy barriers for the SF, ISF, and TF in Ni-Co alloy NWs under three different potentials, where Mishin, Kim and Deluigi refer to the potentials developed by Mishin et al. [157], Kim et al. [159], and Deluigi et al. [158], respectively.

| Co Content, at.% | | 1 | 5 | 10 | 15 | 20 | 30 | 40 | 60 |
|---|---|---|---|---|---|---|---|---|---|
| $\gamma_{USF}$, mJ/m$^2$ | Mishin | 300.21 | 311.09 | 333.11 | 359.68 | 382.55 | 416.98 | 466.51 | 470.36 |
| | Kim | 472.70 | 471.46 | 469.92 | 409.29 | 465.24 | 424.70 | 451.96 | 433.29 |
| | Deluigi | 364.06 | 356.16 | 347.31 | 335.82 | 323.36 | 303.32 | 277.90 | 227.65 |
| $\gamma_{ISF}$, mJ/m$^2$ | Mishin | 136.16 | 147.00 | 172.87 | 204.04 | 229.32 | 263.47 | 326.75 | 326.91 |
| | Kim | 123.33 | 116.79 | 109.88 | 60.94 | 92.55 | 55.40 | 60.59 | 34.42 |
| | Deluigi | 124.69 | 123.75 | 122.19 | 119.58 | 115.86 | 109.56 | 99.56 | 75.76 |
| $\gamma_{UTF}$, mJ/m$^2$ | Mishin | 365.47 | 377.34 | 404.51 | 456.75 | 485.55 | 542.73 | 610.97 | 612.15 |
| | Kim | 546.93 | 542.55 | 537.38 | 449.01 | 523.89 | 463.89 | 498.00 | 464.84 |
| | Deluigi | 433.18 | 424.62 | 416.32 | 403.33 | 390.47 | 369.18 | 343.36 | 283.00 |

For the Ni-Co alloy system, the planar fault energy curves are similar to those for Ni-Cu binary alloy system. All the $\gamma_{USF}$, $\gamma_{ISF}$ and $\gamma_{UTF}$ values are listed in Table 2, respectively. For case-Mishin, all the energy barriers are monotonously increased with higher Co concentration, which indicates that more Co atoms can impede the formation of planar faults. For case-Kim, the energy barriers gradually decrease by increasing the Co concentration from 1 to 60 at.%, except 15 and 30 at.%. However, it follows the general reduction trend for the energy barriers of case-Kim. In contrast to case-Mishin, the energy barriers are monotonously reduced with higher Co concentration. All calculations are performed under the same conditions. Thus, the differences between the results of different potentials can only be attributed to the nature of the potentials.

#### 4.1.4.2 Energy barriers for the MEA and HEA systems

For the MEA systems, the atomic sites in the supercell are randomly occupied by Ni, Fe, and Cu atoms. Similarly, Co, Cr, Ni, Fe, and Cu atoms are randomly distributed inside the HEA supercell for the planar fault energy calculations. All the $\gamma_{USF}$, $\gamma_{ISF}$ and $\gamma_{UTF}$ values for the MEA and HEA systems are listed in Table 3, respectively. All the energy barriers are continuously reduced by increasing the Cu concentration for both alloy systems. For the comparison of two alloy systems, the addition of Co and Cr atoms dramatically decreases each energy barrier for the same Cu concentration, indicating that the existence of Co and Cr atoms reduces the energy barriers both for the formation of SF and TF. Thus, compared to the MEA system, it is easier to nucleate the first partial dislocation when the Cu concentration is the same, which is consistent with the trend of the yield strength for both alloy systems.

As for the difference between the highest energy barriers for SF and TF (Cu-12 at.%) and the lowest one (Cu-48 at.%), the MEA system reveals larger differences in both planar fault energy barriers, which indicates the existence of Co and Cr atoms can slow down the reduction of SF and TF energy barriers caused by increasing the Cu concentration. All the trends can be observed in Table 3.

**Table 3.** Summarized energy barriers for the MEA and HEA systems, where MEA refers to the (NiFe)-Cu$x$ alloy system, and HEA refers to the (CoCrNiFe)-Cu$y$ alloy system.

| Cu Content, at.% | | 12 | 20 | 28 | 40 | 48 |
|---|---|---|---|---|---|---|
| $\gamma_{USF}$, mJ/m$^2$ | MEA | 366.62 | 351.46 | 344.14 | 324.40 | 302.32 |
| | HEA | 280.46 | 277.83 | 268.25 | 257.33 | 256.05 |
| $\gamma_{ISF}$, mJ/m$^2$ | MEA | 85.70 | 78.93 | 77.90 | 70.88 | 59.63 |
| | HEA | 60.76 | 61.93 | 55.80 | 54.19 | 55.16 |
| $\gamma_{UTF}$, mJ/m$^2$ | MEA | 410.56 | 393.05 | 375.74 | 357.86 | 333.97 |
| | HEA | 323.67 | 320.85 | 309.79 | 300.80 | 299.92 |

## 4.2 Results of hybrid MD/MC simulations

### 4.2.1 Results of Ni-based alloy NWs with MD/MC

Hybrid MD/MC simulations have been used to investigate the solute distribution effects on the solid solution softening phenomenon in $\langle 111 \rangle$-oriented Ni-based alloy NWs. As expected, the solute atom distribution has been changed after hybrid MD/MC simulations for Ni-Cu alloy NWs, which can be seen in Figure 28. Apparently, the Cu atoms migrate to the surface of the NW, while Ni atoms concentrate in the center of the NW. Thus, a core-shell structure has been formed by atomic swapping processes, shown in Figure 28. This surface segregation behavior can be attributed to the nature of the free surface of the cylindrical NWs

[172]–[174], which can stabilize the NW by lowering the surface energy, compared to the initial random solute distribution.

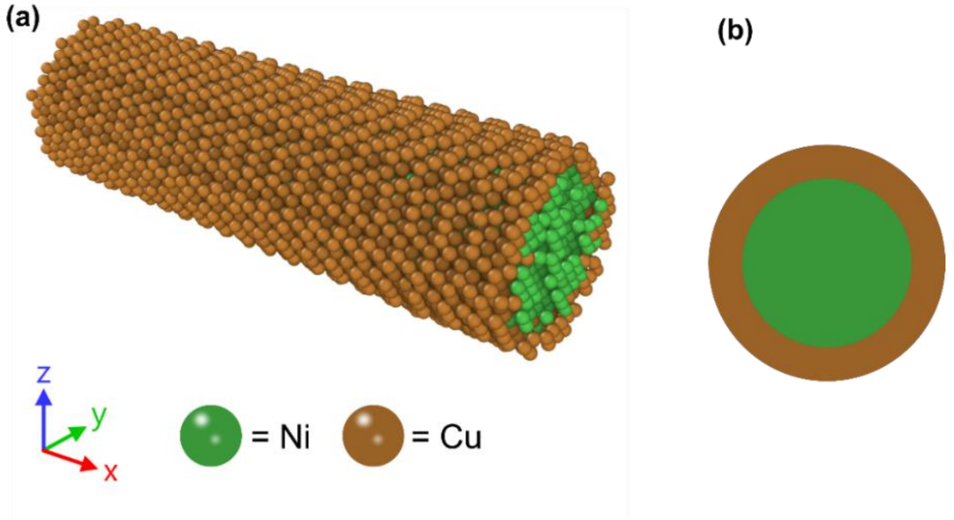

**Figure 28.** Illustration of Ni-Cu NWs after hybrid MD/MC simulations. (a) shows that Cu atoms migrate to the surface of the NW, and Ni atoms are located in the center. (b) shows the schematic core-shell structure of Ni-Cu NWs after hybrid MD/MC simulations.

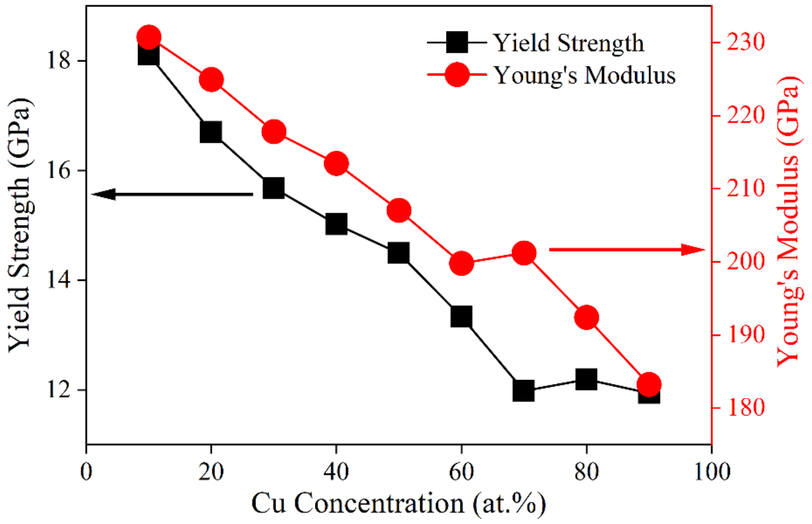

**Figure 29.** Results of uniaxial tensile yield strength and Young's modulus for ⟨111⟩-oriented Ni-Cu alloy NWs after hybrid MD/MC simulations.

After hybrid MD/MC simulations, each ⟨111⟩-oriented Ni-Cu alloy NWs has been uniaxially deformed with a constant strain rate. Each NW yields by the nucleation of $\frac{1}{6}\langle 112\rangle$ partial dislocation, which is the same as solute randomly distributed NWs without hybrid MD/MC simulations. The yield strength and Young's modulus are calculated and shown in

Figure 29 (a) and (b), respectively. The Young's modulus values are obtained by calculating the slope of the strain interval 0~4%. It shows that both yield strength and Young's modulus are monotonously softened by increasing the copper concentration, which is the same as the results of non-MD/MC simulations, indicating that solute distribution has no relation to the softening phenomenon for Ni-Cu alloy NWs, although the model structure has been changed to core-shell after hybrid MD/MC simulations.

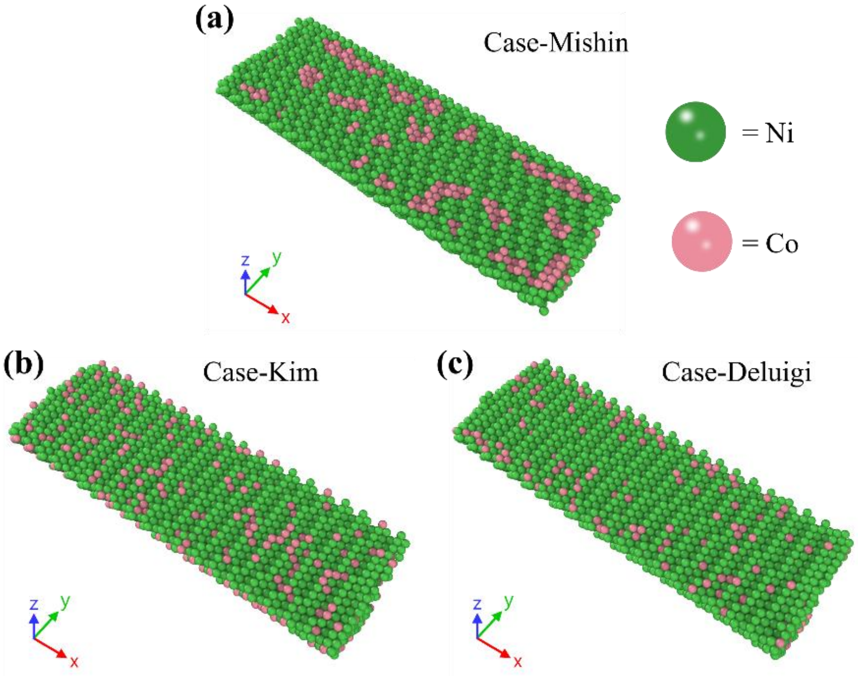

**Figure 30.** Solute distributions after hybrid MD/MC simulations. (a) shows that Co clusters are formed after hybrid MD/MC simulations for case-Mishin. (b) and (c) illustrate that Co atoms are still randomly distributed in the NWs after hybrid MD/MC simulations for case-Kim and -Deluigi, respectively.

As for the ⟨111⟩-oriented Ni-Co alloy NWs, different distribution patterns have been observed under different potentials, shown in Figure 30. It shows the solute distributions under three different potentials after hybrid MD/MC simulations. For case-Mishin, Co small clusters have been formed after hybrid MD/MC simulations. However, solute atoms are still randomly distributed in the NWs for case-Kim and -Deluigi. The difference can only be attributed to the different natures of the potentials.

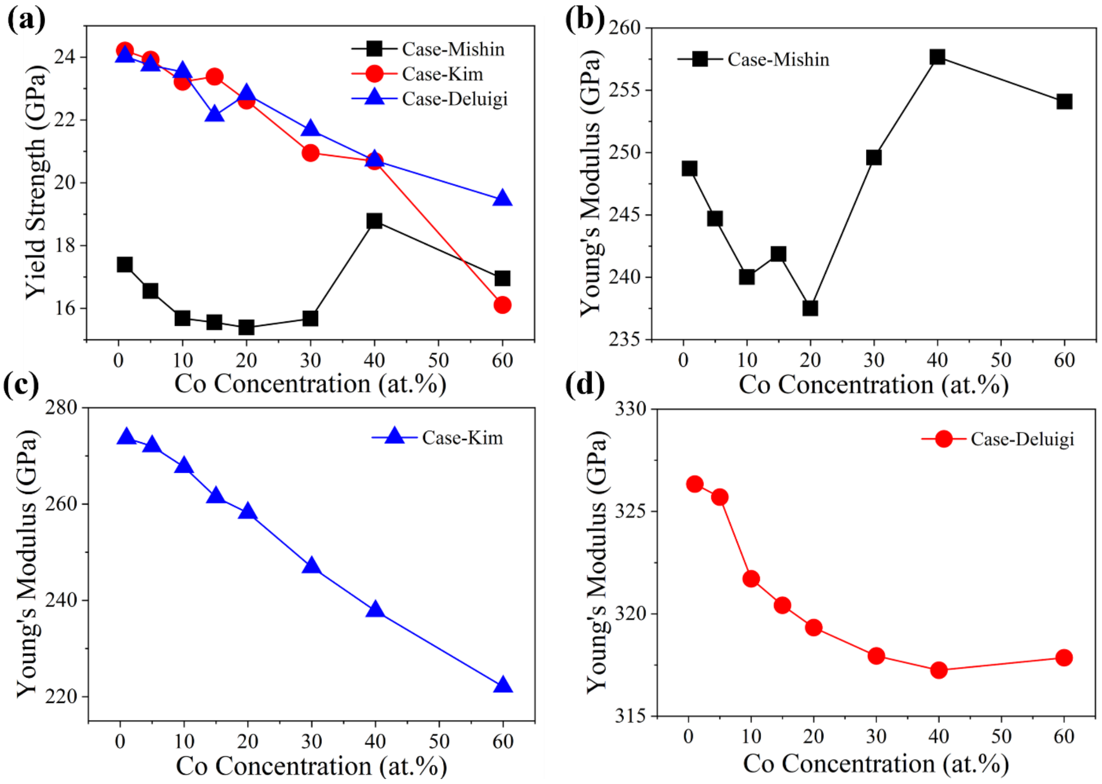

**Figure 31.** Mechanical properties of Ni-Co alloy NWs under three different potentials after hybrid MD/MC simulations. (a) shows the yield strength of three cases. (b), (c) and (d) illustrate the Young's modulus trends against Co concentration of three different cases, respectively.

The mechanical properties of Ni-Co alloy NWs are shown in Figure 31, where (a) shows the variation of yield strength with increased Co concentration. For both case-Kim and -Deluigi, the yield strength has been monotonically softened by increasing the solute concentration, which is consistent with the randomly distributed solute results aforementioned. However, it softens initially with higher Co concentration until 20 at.%, where it reveals the lowest yield strength. Then, the NWs are strengthened by increasing the Co concentration and revealing the highest value at Co-40 at.%, followed by a reduction in yield strength again. The trend for case-Mishin here is dramatically different to the solute randomly distributed case and is also inconsistent with the description in Ref. [140], where it shows monotonous increase trend after the lowest yield strength. The Young's modulus after hybrid MD/MC simulations behaves the same as non-MD/MC cases for both case-Kim and -Deluigi. But it is different from non-MD/MC conditions for case-Mishin. The trend for Young's modulus is similar to the variating behavior of yield strength. The lowest Young's modulus can be observed at Co-20 at.%, while the highest value can be found at Co-40 at.%.

### 4.2.2 Results of Cu-Ag alloy NWs with MD/MC

For the Cu-Ag alloy NWs, the solute distribution has been changed after the hybrid MD/MC simulations, shown in Figure 32 (a) and (b), respectively. When Cu serves as the solute in the NW, there are some small copper clusters formed by the MD/MC process. However, silver atoms will migrate to the surface of the NW after MD/MC, when they serve as the solute atoms. The surface segregation behavior can lower the system energy which makes it more stable compared to the solute random distribution.

The yield strength and Young's modulus of Cu-Ag alloy NWs after hybrid MD/MC simulations are shown in Figure 33 (a) and (b), respectively. For case-Cu-Ag*y*, where Ag is the solute, the yield strength has been greatly reduced from 11.19 GPa at Ag-1 at.% to 7.33 GPa at Ag-10 at.%. Although a monotonous softening phenomenon can also be observed for case-Ag-Cu*x*, it only drops from 4.97 GPa at Cu-1 at.% to 3.74 GPa at Cu-10 at.%, which indicates that the addition of Ag into Cu-NWs has higher influence on yield strength compared to additional Cu atom in Ag-NWs. Similarly, the addition of Cu atoms has less influence on the Young's modulus for case-Ag-Cu*x*, compared to the opposite case. Obvious softening in Young's modulus can only be observed when the Cu concentration is higher than 8 at.%. But for case-Cu-Ag*y*, the Young's modulus is monotonously softened by increasing the Ag concentration, from 175.25 GPa at Ag-1 at.% to 159.66 GPa at Ag-10 at.%. The origination of the softening phenomenon in the Cu-Ag system will be discussed in the next chapter.

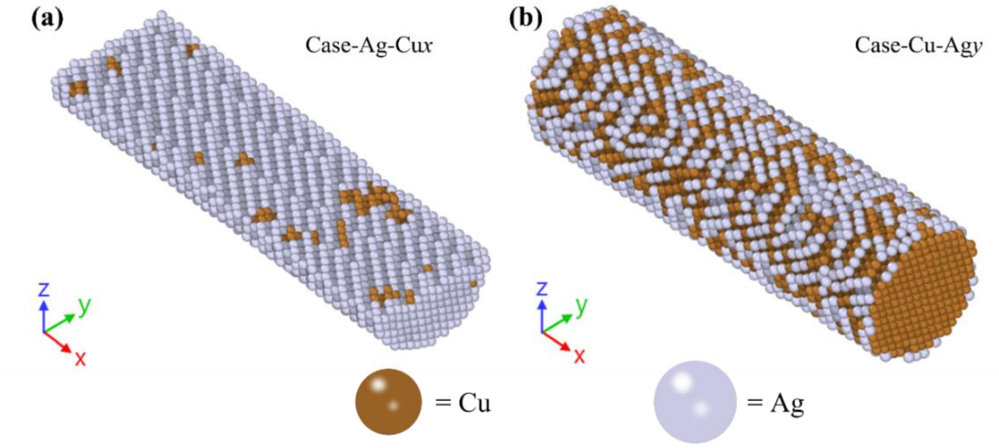

**Figure 32.** Solute distribution of the Cu-Ag alloy NWs after hybrid MD/MC simulations. (a) and (b) refer to the case-Ag-Cu*x* and case-Cu-Ag*y*, respectively.

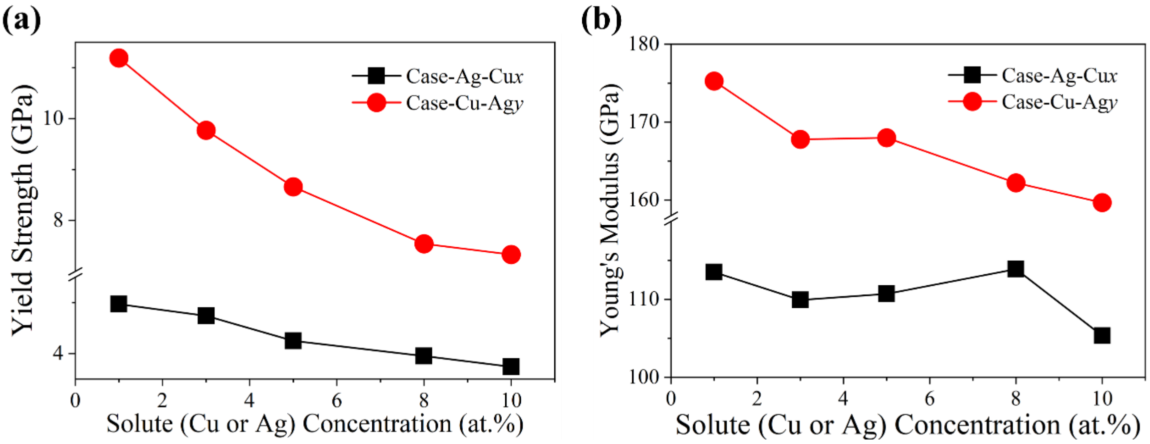

**Figure 33.** Mechanical properties of Cu-Ag alloy NWs after hybrid MD/MC simulations. (a) and (b) illustrate the yield strength and Young's modulus variations with increasing the solute concentration, respectively.

### 4.2.3 Results of Mg-Al system

For case-Mg-Al*x*, whose initial structure is hcp, Al atoms will concentrate in some regions, shown in Figure 34 (a). However, phase transformation can be observed when the Al concentration is equal to or higher than 6 at.%, shown in Figure 34 (b). No secondary phase can be formed by hybrid MD/MC simulations when the solute (Al) concentration is lower than 10 at.%. Moreover, the surface becomes unsmooth near the regions where phase transformation happens, indicating that dislocations may exist after the MD/MC treatment. As for case-Al-Mg*y*, solute (Mg) atoms migrate to the surface of the NW, and homogeneously distribute at the outmost shell, shown in Figure 34 (c). In the meantime, Al atoms will concentrate inside the alloy NW. According to the CNA, all the NWs are still kept pure fcc structure after hybrid MD/MC simulations, even the solute (Mg) concentration comes to 12 at.%. No residual dislocations can be observed before the yielding of the case-Al-Mg*y* alloy NWs.

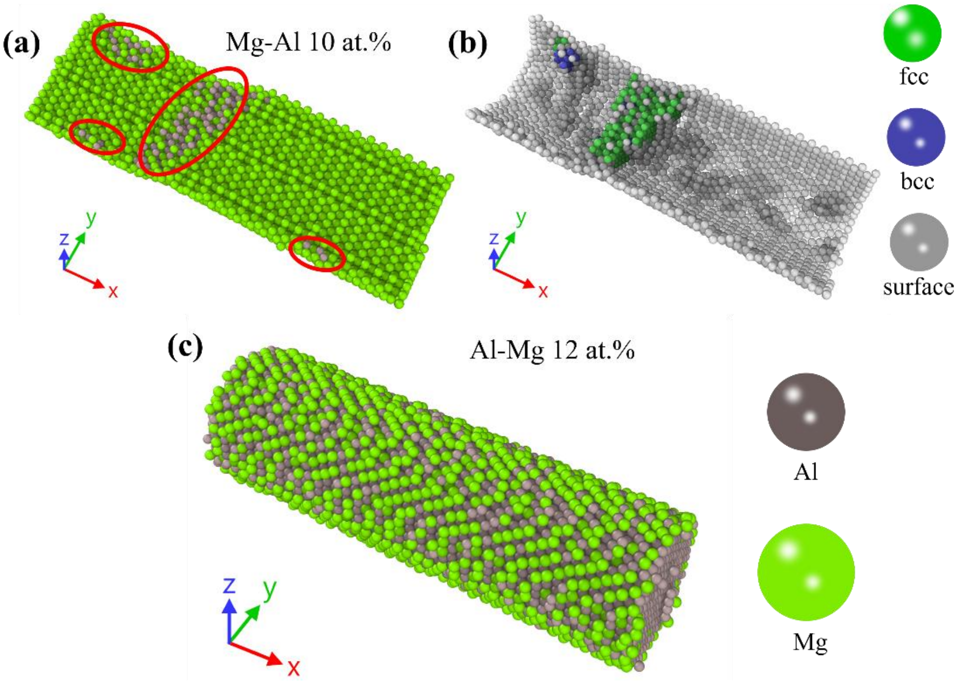

**Figure 34.** Structures of Mg-Al*x* and Al-Mg*y* NWs after hybrid MD/MC simulations. (a) shows the solute (Mg-Al 10 at.%) atoms concentrate in some regions which have been circled by red voals. (b) shows that bcc, fcc and amorphous phases have been formed after hybrid MD/MC simulations of the Mg-Al 10 at.% NW. (c) indicates that Mg atoms migrate to the surface of the NW after hybrid MD/MC simulation for Al-Mg 12 at.%.

The mechanical properties of the Mg-Al alloy NWs are shown in Figure 35. For case-Mg-Al*x*, strain hardening can be observed, especially when the Al concentration is higher than 4 at.%, shown in Figure 35 (a). Moreover, residual dislocations can be observed in NWs when Al concentration is higher than 6 at.%. Thus, the yield strength can be obtained by the 0.2% offset method. In contrast, obvious yielding behavior can be observed in case-Al-Mg*y*, shown in Figure 35 (b), which means that the yield stress can be considered as the yield strength. The yield strength for both cases is shown in Figure 35 (c). Apparently, the yield strength for both cases has been softened by increasing the solute concentration, although there is no obvious reduction in the yield strength when the Mg concentration is lower than 6 at.% for case-Al-Mg*y*. And for case-Mg-Al*x*, an obvious reduction in yield strength can be observed at any solute concentration interval. As for the Young's modulus, it is softened with higher Al concentration for case-Mg-Al*x*, although there are some fluctuations for higher solute concentration. However, for case-Al-Mg*y*, the Young's modulus softened from 97.48 GPa at Mg-2 at.% to 89.43 GPa at Mg-4 at.%, then it is gradually strengthened to 97.03 GPa at Mg-8 at.%. Finally, the Young's modulus is continuously softened to 81.56 GPa at Mg-12 at.%.

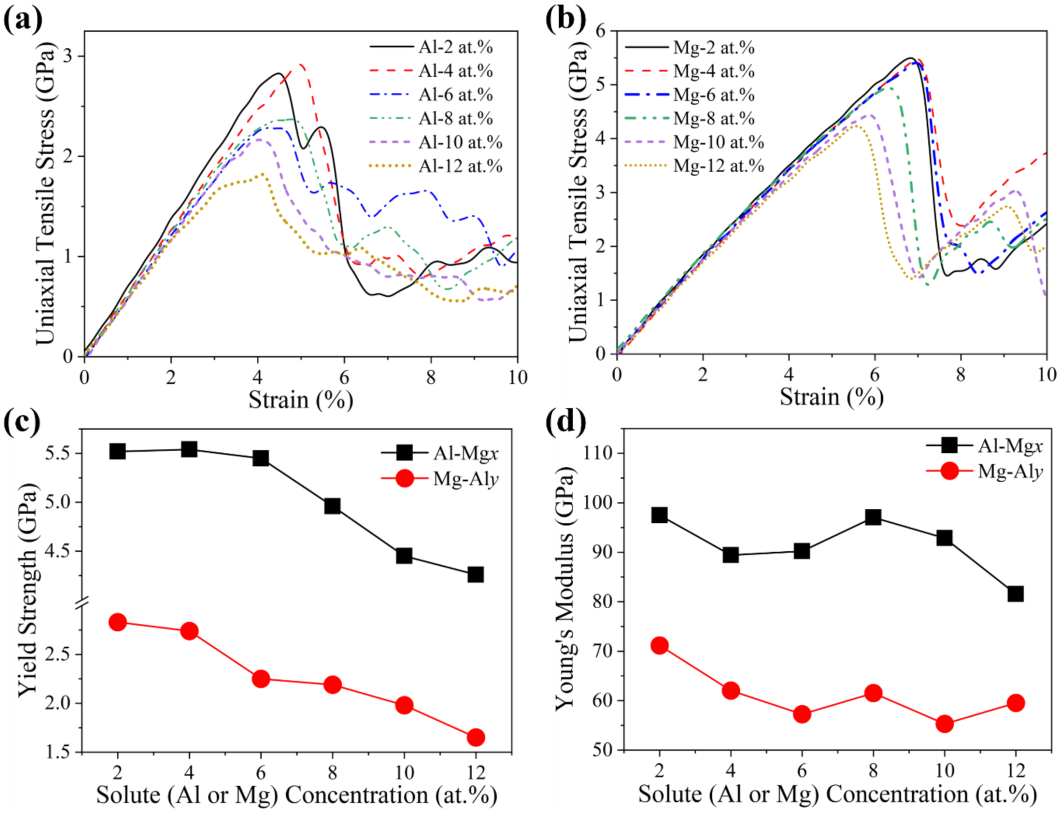

**Figure 35.** Mechanical properties after hybrid MD/MC simulations of Mg-Al binary alloy NWs. (a) and (b) are the stress-strain curves of case-Mg-Al*x* and case-Al-Mg*y*, respectively. (c) and (d) represent the yield strength and Young's modulus for both cases, respectively.

## 4.3 Discussions

### 4.3.1 Softening in Ni-based alloy NWs

As described in section 4.1.1, both yield strength and Young's modulus are monotonously reduced by increasing the Cu concentration, which indicates the alloy NWs are softened by adding more copper atoms. All the Ni-Cu alloy NWs, pure Ni and Cu NWs are yielded by the nucleation of $\frac{1}{6}\langle 112\rangle$ partial dislocation, no matter what the NW orientation is, which is consistent with the work done by Park et al. [97]. Nevertheless, the nucleation of the partial dislocation is controlled by the energy barrier for the formation of a SF [162].

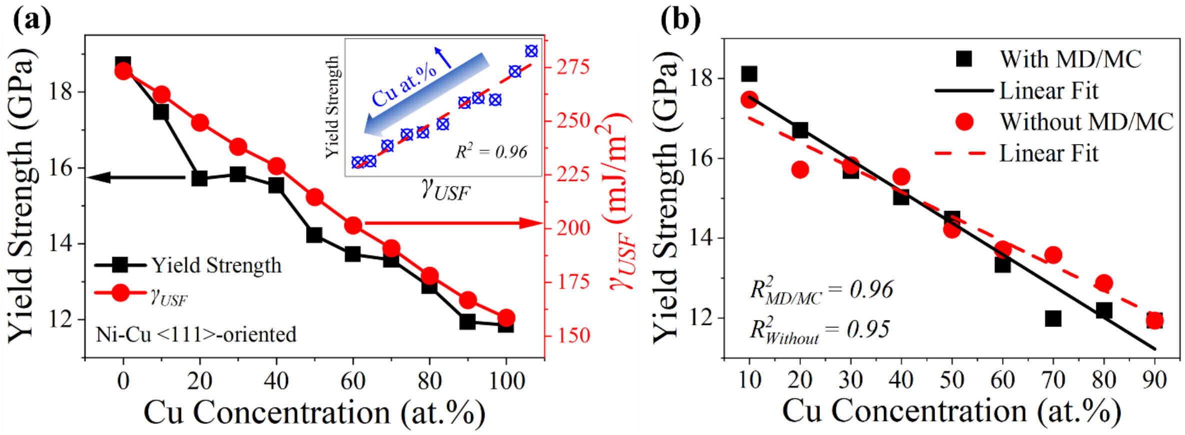

**Figure 36.** (a) shows the relationship of yield strength and unstable stacking fault energy $\gamma_{USF}$ with solute (Cu) concentration. The insert shows the linear relationship between yield strength and $\gamma_{USF}$. (b) shows the Comparison of the yield strength of the $\langle 111\rangle$-oriented Ni-Cu alloy NWs between with and without hybrid MD/MC simulations.

As is shown in Figure 36 (a), both yield strength and unstable stacking fault energy $\gamma_{USF}$ are monotonically reduced with Cu concentration increase, although there are some fluctuations in yield strength. Thus, the yield strength of the Ni-Cu NWs will be strengthened if reducing the Cu concentration, in turn. So does for the $\gamma_{USF}$. The insert diagram indicates that the yield strength and $\gamma_{USF}$ are linearly related to each other, which confirms that the softening of Ni-Cu NWs originates from the reduction of $\gamma_{USF}$ by increasing the Cu concentration. Thus, the addition of copper atoms facilitates the nucleation of the $\frac{1}{6}\langle 112\rangle$ partial dislocation, which induces the softening phenomenon that happens in the alloyed Ni-Cu NWs. For the NWs after MD/MC simulations, the yield strength is also linearly softened by increasing the Cu concentration, shown in Figure 36 (b) , which means that the addition of Cu atoms softens the NWs even though the solute distribution has been changed.

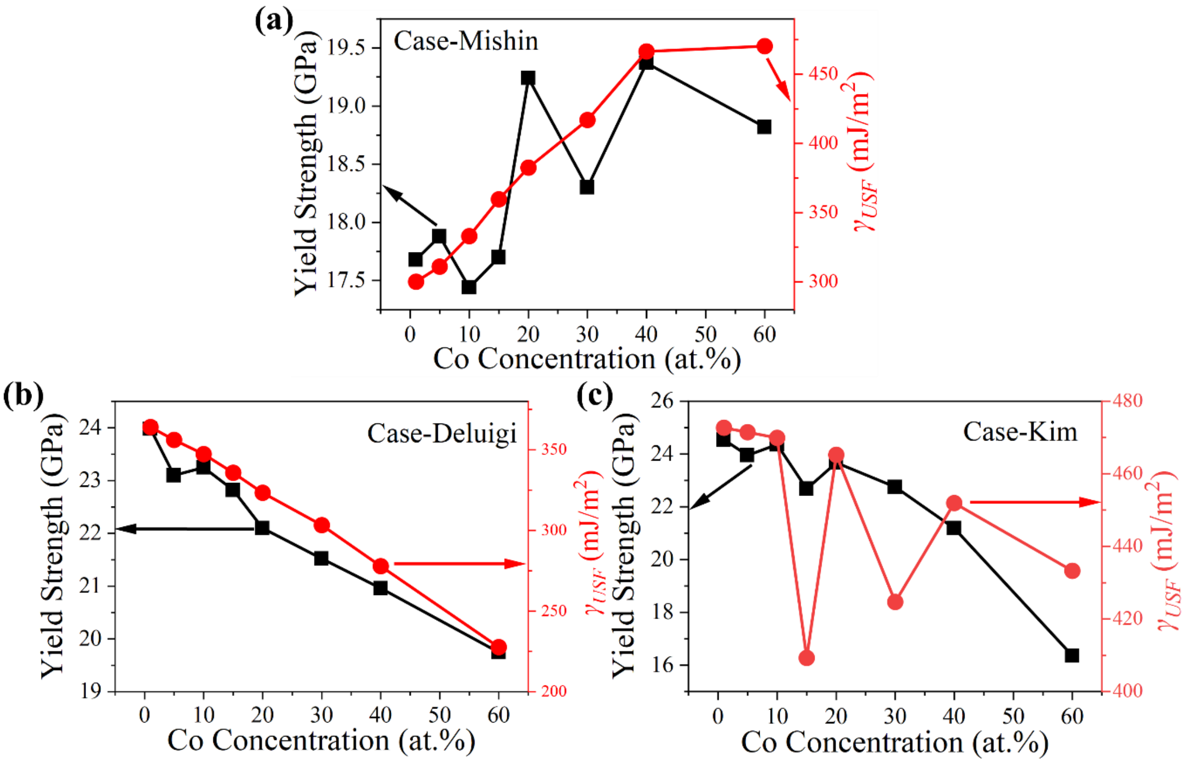

**Figure 37.** Results of yield strength and $\gamma_{USF}$ vs Co concentration of three different cases. (a), (b) and (c) illustrate the trend of both yield strength and SF energy barriers for case-Mishin, case-Deluigi and case-Kim, respectively.

The yield strength and $\gamma_{USF}$ versus solute concentration behaviors of three different case Ni-Co alloy NWs are shown in Figure 37. Accordingly, all three cases reveal that the yield strength and $\gamma_{USF}$ follow the same overall relationship with solute concentration, although there are some dramatic deviations in some $\gamma_{USF}$ or yield strength values, for instance, the dramatic fluctuations in yield strength for case-Mishin-random compared to its $\gamma_{USF}$ values, and great deviations in $\gamma_{USF}$ values for case-Kim-random compared to its yield strength. While the case-Deluigi-random behaves like the Ni-Cu NWs, both yield strength and $\gamma_{USF}$ are monotonously reduced with increasing the Co concentration. Thus, all these results indicate that the $\gamma_{USF}$ is an important, but not the only parameter for determining the yield strength. There must be other parameters that control the yielding behavior of the NWs.

As for the Ni-Co NW models after hybrid MD/MC simulations, the yield strength for both case-Kim-MD/MC and case-Deluigi-MD/MC behave the same as non-MD/MC cases. However, the yield strength-Co concentration curve has been dramatically changed after MD/MC treatment, which indicates that the solute distribution does affect the nucleation of the first partial dislocation. In this work, all the Ni-based alloy NWs yield by the mechanism of surface nucleation of first partial dislocation, and the $\gamma_{USF}$ is believed to be the energy barrier of a partial dislocation [162]. It has been reported that atomic friction stress [139], [140] and atomic lattice distortion [175] may also affect the yielding behavior of fcc metals. As described by Bisht et al. [140], the atomic friction will affect the dislocation motion after its first nucleation, which causes the transition from softening to strengthening in the Ni-Co alloy nanoparticles with higher Co concentration. However, this description cannot explain the transition from softening to strengthening in MD/MC treated Ni-Co alloy NWs in case-Mishin-MD/MC, since the yielding happens when the nucleation of the first dislocation occurs, and no strain hardening can be observed, which means that atomic friction can enhance the yield strength in this scenario.

The atomic size misfit $\delta$ values are calculated using Eq. (8) and (9) [176]:

$$\delta = \sqrt{\sum_{i=1}^{n} c_i \left(1 - \frac{r_i}{\bar{r}}\right)^2} \qquad \text{Eq. (8)}$$

$$\bar{r} = \sum_{i=1}^{n} c_i r_i \qquad \text{Eq. (9)}$$

where, n indicates the number of elements; $i$ represents the $i$th element; $c_i$ is the atomic fraction of the $i$th element; $r_i$ is the radius of the $i$th element; and $\bar{r}$ is the average atomic radius of the system, which is evaluated by Eq. (9). The atomic radius for Ni and Co are taken from the Ref. [177], which are 124 pm and 125 pm, respectively. For each Co concentration ranging from 1 to 60 at.%, the atomic size misfit is lower than 0.4%, which is a relatively negligible value. Thus, the strengthening for case-Mishin-random and softening for case-Kim-random and -Deluigi-random can all be explained by the increase and reduction in $\gamma_{USF}$.

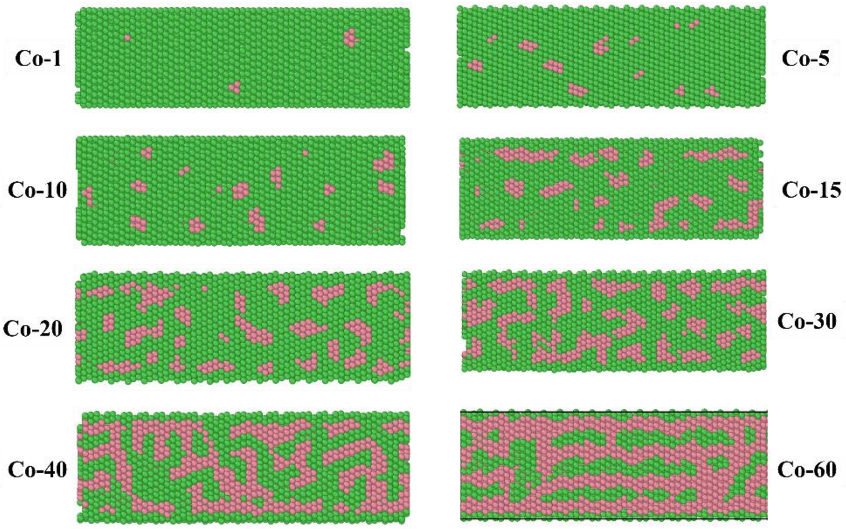

**Figure 38.** Solute Co distribution after hybrid MD/MC simulations for each Ni-Co alloy NW model for case-Mishin. Small clusters can be observed.

The softening in case-Mishin-MD/MC when Co concentration ranges from 1 to 20 at.% can be explained by the clustering of solute atoms. After hybrid MD/MC simulations, there are some small clusters inside the NW model. Larger clusters can be obtained by increasing the Co concentration, as shown in Figure 38. And these clusters are believed to decrease the nucleation barrier of the first partial dislocation in such single crystal NWs, because of the reduction in host-solute bonds which can reinforce the NWs by increasing the $\gamma_{USF}$. Thus, the transition from softening to strengthening can be explained by the competing of two opposite effects: first, clustering softens the partial dislocation nucleation energy barrier which dominates the softening in case-Mishin-MD/MC when the solute concentration is lower than the critical value; second, higher solute concentration enhances the $\gamma_{USF}$ values, which may increase the energy barrier of first partial nucleation and dominates the solute strengthening behavior.

### 4.3.2 Softening in MEA and HEA NWs

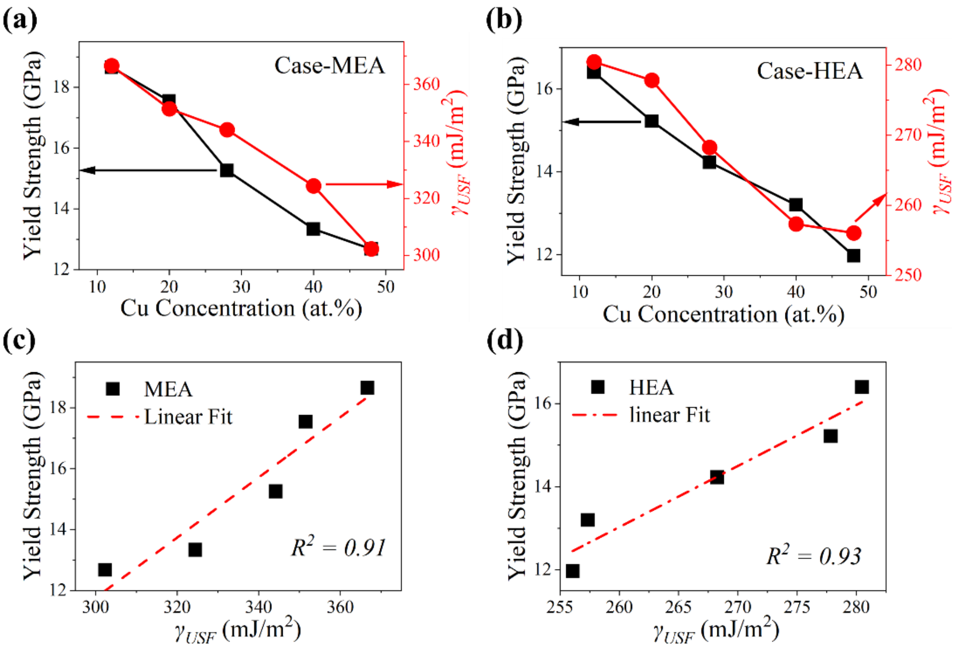

**Figure 39.** Softening in MEA and HEA NWs. (a) and (b) show that both yield strength and $\gamma_{USF}$ are monotonously reduced by increasing the Cu concentration for case-MEA and -HEA, respectively. (c) and (d) represent the relationship between yield strength and $\gamma_{USF}$ for both cases, respectively.

In the solute randomly distributed MEA NWs and HEA NWs, the yield strength is the same as the stress when the first partial is formed. Both yield strength and $\gamma_{USF}$ for each case are monotonously reduced by increasing the solute concentration from 12 to 48 at.%, which can be seen from Figure 39 (a) and (b), which shows the similarity with Ni-Cu alloy NWs. The relationship between yield strength and $\gamma_{USF}$ are shown in Figure 39 (c) and (d) for case-MEA and -HEA, respectively. Apparently, they are linearly related to each other in both cases, which indicates that the softening in the MEA and HEA NWs can be attributed to the reduction of $\gamma_{USF}$, the partial dislocation nucleation energy barrier, by increasing the Cu concentration. Comparing the $\gamma_{USF}$ values for both cases, each MEA model has much higher dislocation energy barrier than its counterparts of HEA NWs with the same Cu concentration, which also confirms that the addition of Co and Cr atoms, and reduction of Ni atoms at the same Cu concentration will soften the NW as well.

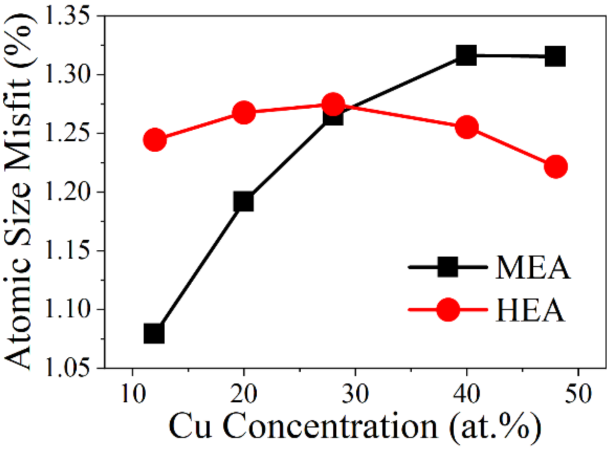

**Figure 40.** Atomic size misfit calculated results for case-MEA and -HEA NWs. For both cases, the variation of atomic size misfit is relatively small and negligible, especially for case-HEA.

The atomic size misfit calculated by Eq. (8) and (9) for both cases is shown in Figure 40, where the atomic radius values are taken from Ref. [177], for Co 125 pm, Cr 128 pm, Ni 124 pm, Fe 126 pm, and Cu 128 pm. It shows that the atomic size misfit for case-MEA becomes larger from 1.08% at Cu-12 at.% to 1.32% at Cu-40 and 48 at.%. The variation is relatively small and negligible for both cases, especially for case-HEA. But the atomic size misfit can be used to explain the slight deviation of the yield strength with the increase of Cu concentration. For instance, the slope of yield strength vs Cu concentration for the interval of Cu-12 to 20 at.% is smaller than the interval of Cu-20 to 40 at.%, which can be attributed to the smaller atomic size misfit value in the initial Cu concentration interval. Thus, the primary softening origination in the MEA and HEA NWs in this work is due to the lower $\gamma_{USF}$ caused by adding more Cu atoms. The atomic size misfit has a very finite effect on the yielding behavior of the MEA and HEA NWs.

### 4.3.3 Softening in Cu-Ag alloy NWs

Softening phenomenon can also be observed in the immiscible alloy system Cu-Ag. However, with either Cu or Ag as the solute atoms, the alloyed NWs are all softened with higher solute concentration, which is dramatically different to the monotonous softening in Ni-Cu alloy NWs. To investigate the softening originations in Cu-Ag alloy NWs, the generalized planar fault energies have also been calculated by using the same method described in section 3.2.4. The results are shown in Table 4. For case-Ag-Cu$x$, by varying the Cu concentration from 1 to 10 at.%, the $\gamma_{USF}$ values only reduce from 112.83 to 110.00 mJ/m$^2$, which is negligible compared to the variation of $\gamma_{USF}$ caused by increasing Ag atoms for case-Cu-Ag$y$, varying from 160.00 to 144.01 mJ/m$^2$. Thus, the softening effect caused by variation of $\gamma_{USF}$ for case-Ag-Cu$x$ is negligible.

To evaluate the influence of atomic size misfit, the $\delta$ values for both cases have been calculated by using Eq. (8) and (9), where the atomic radii, Cu for 128 pm and Ag for 144 pm, are taken from Ref. [177]. The results of atomic size misfit are shown in Figure 41 (a) and (b) for case-Ag-Cu$x$ and -Cu-Ag$y$, respectively. Apparently, the atomic size misfit has been enhanced by increasing solute concentration, while the yield strength is reduced for both cases, which follows the statement that atomic size misfit aids the nucleation of the first partial dislocation for single crystalline MNWs. The atomic size misfit is much more significant to induce softening phenomenon, compared to the values for the Ni-based alloy, MEA, and HEA cases.

**Table 4.** Summarized planar fault energies for Cu-Ag alloy system.

| Solute (Cu or Ag) Content, at.% | | 1 | 3 | 5 | 8 | 10 |
|---|---|---|---|---|---|---|
| $\gamma_{USF}$, mJ/m$^2$ | Ag-Cu$x$ | 112.83 | 112.50 | 111.83 | 110.80 | 110.00 |
| | Cu-Ag$y$ | 160.00 | 150.93 | 149.54 | 148.35 | 144.01 |
| $\gamma_{ISF}$, mJ/m$^2$ | Ag-Cu$x$ | 21.12 | 19.67 | 18.08 | 16.46 | 14.47 |
| | Cu-Ag$y$ | 49.35 | 45.28 | 42.92 | 42.32 | 38.52 |
| $\gamma_{UTF}$, mJ/m$^2$ | Ag-Cu$x$ | 125.59 | 124.18 | 122.15 | 120.97 | 118.42 |
| | Cu-Ag$y$ | 185.15 | 177.24 | 172.4 | 174.03 | 39.38 |

As described previously, the variation of $\gamma_{USF}$ is negligible for case-Ag-Cu$x$, which means that the atomic size misfit dominates the softening phenomenon in Ag-Cu alloy NWs, confirmed by Figure 41 (c). It shows the relationship between yield strength and atomic size misfit for case-Ag-Cu$x$. Obviously, they are negatively and linearly related to each other with the R-square value as high as 0.97, indicating that the yield strength is highly dependent on the atomic size misfit for Ag-Cu alloy NWs.

For case-Cu-Ag$y$, Figure 41 (d) and (e) illustrate the relationship between yield strength and atomic size misfit, and the relationship between yield strength and $\gamma_{USF}$, respectively. Figure 41 (d) indicates that the yield strength is negatively and linearly related to the atomic size misfit with the R-square value as high as 0.99. However, the variation of $\gamma_{USF}$ is much more significant compared to the case-Ag-Cu$x$ and has a positive effect on the yield strength.

But the R-square value is only 0.88, which is much lower than the value for atomic size misfit. Hence, the softening in Cu-Ag alloy NWs has two sources: first, the reduction of $\gamma_{USF}$ caused by increasing Ag concentration; second, the increase of atomic size misfit with higher Ag concentration. Nevertheless, the atomic size misfit dominates the softening phenomenon in Cu-Ag alloy NWs.

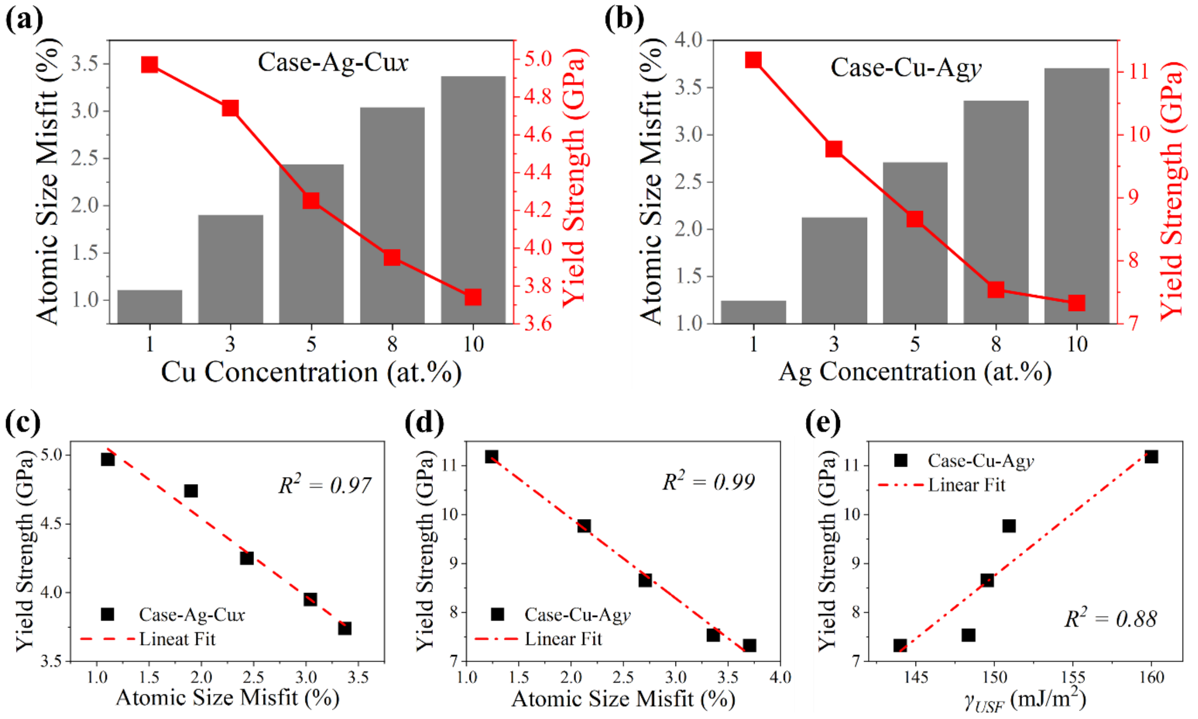

**Figure 41.** Results of Cu-Ag alloy NWs. (a) and (b) represent the relationship between atomic size misfit and the solute concentration, and the relationship between yield strength and solute concentration for both cases, respectively. (c) and (d) illustrate the relationship between yield strength and atomic size misfit for both cases, respectively. (e) shows the relationship between yield strength and $\gamma_{USF}$ for case-Cu-Ag$y$.

### 4.3.4 Softening in Mg-Al alloy NWs

For the case-Mg-Al$x$, where Al atoms serve as the solute, the softening in yield strength can be attributed to the combined effect of phase transformation and atomic size misfit. The atomic size misfit for both cases is calculated by Eq. (8) and (9), and the atomic radii 160 pm for Mg and 143 pm for Al are taken from Ref. [177]. Figure 42 (a) shows that higher atomic size misfit causes softening in yield strength. Figure 42 (c) confirms that the yield strength of Mg-Al*x* NWs is highly dependent on the atomic size misfit. Another factor may also affect the yield strength of case-Mg-Al*x*, which is the formation of a secondary phase and the solute clustering described in section 4.2.3.

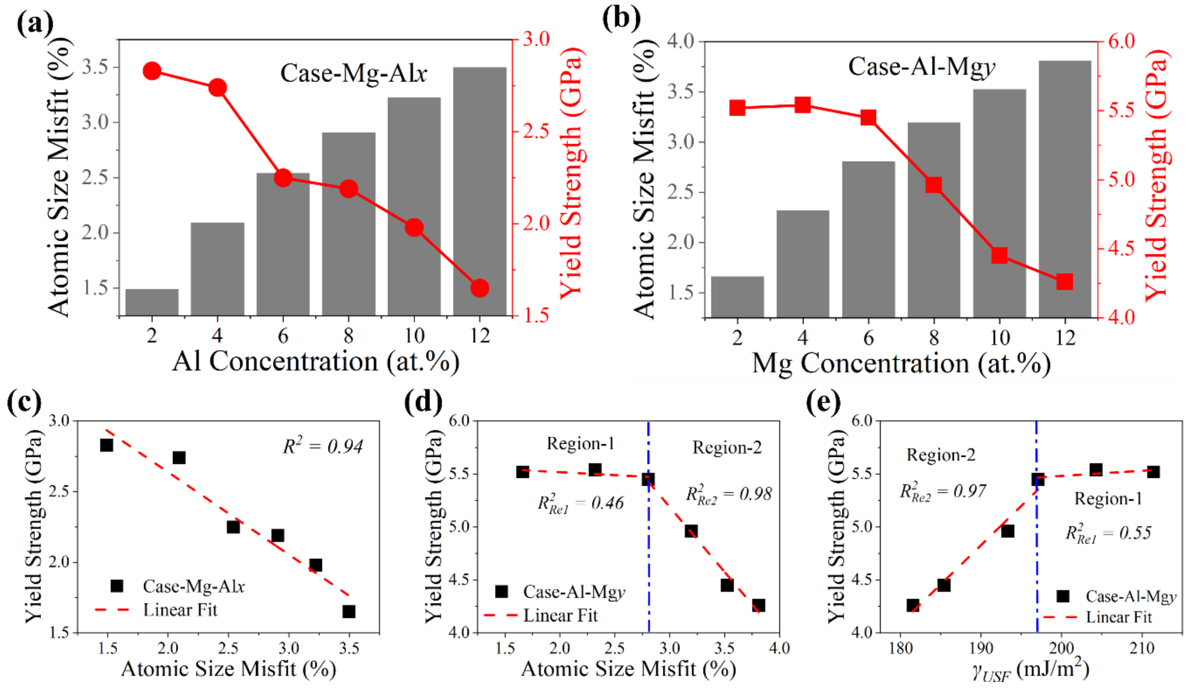

**Figure 42.** Results of Al-Mg alloy NWs. (a) and (b) show the relationship between atomic size misfit and solute concentration, and the relationship between yield strength and solute concentration for case-Mg-Al*x* and case-Al-Mg*y*, respectively. (c), (d) and (e) illustrate the correlation between yield strength and atomic size misfit and $\gamma_{USF}$ for both cases, respectively. The $\gamma_{USF}$ values are obtained by using the same calculation method described in section 3.2.4.

For case-Al-Mg*y*, after hybrid MD/MC simulations, solute atoms migrate to the surface of the NWs, which reduces the host-solute bonding. This can be used to explain the very slight variation of yield strength until the solute concentration comes to Mg-6 at.%, after which obvious softening can be observed. The results are shown in Figure 42 (b), (d), and (e). There are two regions in both Figure 42 (d) and (e), where Region-1 refers to the solute concentration no more than 6 at.%. While Region-2 refers to the rest cases, where the yield strength is dramatically softened by increasing solute concentration in both cases. In Region-1 for both cases, the yield strength is less dependent on either atomic size misfit or the $\gamma_{USF}$. However, the yield strength is highly dependent on both atomic size misfit and $\gamma_{USF}$ in Region-2, with the R-square values as high as 0.98 and 0.97, respectively. In this occasion, since the Mg atoms migrate to the surface, the atomic size misfit is enhanced at the free surface, where partial dislocations are formed. Hence, the enhanced atomic size misfit facilitates the nucleation of the first partial dislocation, which induces the yield behavior.

# Chapter V Conclusions

In summary, the alloying-induced softening phenomenon has been investigated in single crystalline metal nanowires for different alloy systems by using MD simulations and combined with hybrid MD/MC simulations in some cases. The results are interesting and somewhat unexpected. The underlying softening mechanisms for different alloy systems have also been discussed. Five major conclusions can be made based on the results of this work:

1. The alloying-induced softening phenomenon can be widely observed in single crystalline metal nanowires.
2. Two major sources have been found to soften the alloy MNWs: the composition variation-induced reduction in stacking fault energy barrier and the increase in atomic size misfit. Both are found to affect the nucleation of the first partial dislocation which controls the yielding behavior of the single crystalline alloy MNWs.
3. For the low atomic size misfit alloy systems, for instance, the Ni-Cu alloy, MEA, and HEA NWs, more solute atoms will cause the reduction of $\gamma_{USF}$, which can facilitate the nucleation of first partial dislocation and dominate the softening behavior.
4. In the immiscible Cu-Ag alloy systems, the atomic size misfit dominates the softening behavior when Cu atoms serve as the solute, since the reduction of $\gamma_{USF}$ caused by increasing solute concentration is negligible. While a combined effect of two mechanisms has been found in the alloy NWs when Ag atoms are the solute.

5. Moreover, solute segregation and clustering may also cause softening phenomenon, for instance, the case-Mishin of Ni-Co alloy NWs and the Mg-Al alloy NWs.

It is worth noting that the Young's modulus can be monotonically softened by adding more solute atoms, such as the softening of Young's modulus in Ni-Cu, MEA, and HEA NWs. More generally, the transition between softening and strengthening in Young's modulus has been observed in Ni-Co, Ag-Cu, and Mg-Al alloy NWs. Most of the Young's modulus versus composition follows a similar trend with yield strength-solute concentration behavior. However, more work needs to be done to investigate the Young's modulus behaviors by varying the solute concentration in the future.

# Reference

[1] R. P. Feynman, "Plenty of Room at the Bottom," in *APS annual meeting*, 1959.

[2] H. Yu, J.-Y. Park, C. W. Kwon, S.-C. Hong, K.-M. Park, and P.-S. Chang, "An Overview of Nanotechnology in Food Science: Preparative Methods, Practical Applications, and Safety," *Journal of Chemistry*, vol. 2018, pp. 1–10, Oct. 2018, doi: 10.1155/2018/5427978.

[3] X. He, H. Deng, and H. Hwang, "The current application of nanotechnology in food and agriculture," *Journal of Food and Drug Analysis*, vol. 27, no. 1, pp. 1–21, Jan. 2019, doi: 10.1016/j.jfda.2018.12.002.

[4] M. H. Ahmadi *et al.*, "Renewable energy harvesting with the application of nanotechnology: A review," *International Journal of Energy Research*, vol. 43, no. 4, pp. 1387–1410, 2019, doi: 10.1002/er.4282.

[5] A. Awad, W. Ahmed, and M. Waleed, "Chapter 18 - Nanotechnology for energy storage," in *Emerging Nanotechnologies for Renewable Energy*, W. Ahmed, M. Booth, and E. Nourafkan, Eds. Elsevier, 2021, pp. 495–516. doi: 10.1016/B978-0-12-821346-9.00009-2.

[6] C. J. Gardner *et al.*, "Controlled metallic nanopillars for low impedance biomedical electrode," *Acta Biomaterialia*, vol. 10, no. 5, Art. no. 5, May 2014, doi: 10.1016/j.actbio.2013.12.046.

[7] S. Bashir and J. Liu, "Nanomaterials and Their Application," in *Advanced Nanomaterials and their Applications in Renewable Energy*, Elsevier, 2015, pp. 1–50. doi: 10.1016/B978-0-12-801528-5.00001-4.

[8] E. I. Akpan, X. Shen, B. Wetzel, and K. Friedrich, "Design and Synthesis of Polymer Nanocomposites," in *Polymer Composites with Functionalized Nanoparticles*, Elsevier, 2019, pp. 47–83. doi: 10.1016/B978-0-12-814064-2.00002-0.

[9] D. Appell, "Escaping the Earth's gravitational clutches by climbing up a long rope made from carbon nanotubes is a pretty madcap idea. But, as David Appell found out from a recent 'space elevator' conference, there are plenty of enthusiasts out there who are determined to make the concept work," p. 6, 2011.

[10] M. MInus and S. Kumar, "The processing, properties, and structure of carbon fibers," *JOM*, vol. 57, no. 2, pp. 52–58, Feb. 2005, doi: 10.1007/s11837-005-0217-8.

[11] H. G. Chae and S. Kumar, "Rigid-rod polymeric fibers," *Journal of Applied Polymer Science*, vol. 100, no. 1, pp. 791–802, 2006, doi: 10.1002/app.22680.

[12] Y. Bai *et al.*, "Carbon nanotube bundles with tensile strength over 80 GPa," *Nature Nanotech*, vol. 13, no. 7, pp. 589–595, Jul. 2018, doi: 10.1038/s41565-018-0141-z.

[13] A. Sato and M. Meshii, "Solid solution softening and solid solution hardening," *Acta Metallurgica*, vol. 21, no. 6, pp. 753–768, Jun. 1973, doi: 10.1016/0001-6160(73)90040-0.

[14] "nanowire | nanotechnology | Britannica." https://www.britannica.com/technology/nanowire (accessed Aug. 22, 2022).

[15] J.-P. Colinge, *Silicon-on-Insulator Technology: Materials to VLSI: Materials to Vlsi*. Springer Science & Business Media, 2004.

[16] O. D. Neikov and N. A. Yefimov, "Chapter 9 - Nanopowders," in *Handbook of Non-Ferrous Metal Powders (Second Edition)*, O. D. Neikov, S. S. Naboychenko, and N. A. Yefimov, Eds. Oxford:

Elsevier, 2019, pp. 271–311. doi: 10.1016/B978-0-08-100543-9.00009-9.

[17] S. Itoua and C. Joachim, “Fabrication and AFM characterization of gold wires of less than 50 nm width buried in a $SiO_2$ substrate,” *Nanotechnology*, vol. 3, no. 1, pp. 10–15, Jan. 1992, doi: 10.1088/0957-4484/3/1/003.

[18] P. M. Ajayan and S. Iijima, “Capillarity-induced filling of carbon nanotubes,” *Nature*, vol. 361, no. 6410, pp. 333–334, Jan. 1993, doi: 10.1038/361333a0.

[19] T. M. Whitney, P. C. Searson, J. S. Jiang, and C. L. Chien, “Fabrication and Magnetic Properties of Arrays of Metallic Nanowires,” *Science*, vol. 261, no. 5126, pp. 1316–1319, Sep. 1993, doi: 10.1126/science.261.5126.1316.

[20] D. V. M. Arole and S. V. Munde, “FABRICATION OF NANOMATERIALS BY TOP-DOWN AND BOTTOM-UP APPROACHES – AN OVERVIEW,” vol. 1, no. 2, p. 5, 2014.

[21] N. Abid *et al.*, “Synthesis of nanomaterials using various top-down and bottom-up approaches, influencing factors, advantages, and disadvantages: A review,” *Advances in Colloid and Interface Science*, vol. 300, p. 102597, Feb. 2022, doi: 10.1016/j.cis.2021.102597.

[22] D. Mijatovic, J. C. T. Eijkel, and A. van den Berg, “Technologies for nanofluidic systems: top-down vs. bottom-up—a review,” *Lab Chip*, vol. 5, no. 5, p. 492, 2005, doi: 10.1039/b416951d.

[23] P. Iqbal, J. A. Preece, and P. M. Mendes, “Nanotechnology: The ‘Top-Down’ and ‘Bottom-Up’ Approaches,” in *Supramolecular Chemistry*, P. A. Gale and J. W. Steed, Eds. Chichester, UK: John Wiley & Sons, Ltd, 2012, p. smc195. doi: 10.1002/9780470661345.smc195.

[24] R. Kitaura, N. Imazu, K. Kobayashi, and H. Shinohara, “Fabrication of Metal Nanowires in Carbon Nanotubes via Versatile Nano-Template Reaction,” *Nano Lett.*, vol. 8, no. 2, pp. 693–699, Feb. 2008, doi: 10.1021/nl073070d.

[25] Y. Konishi, M. Motoyama, H. Matsushima, Y. Fukunaka, R. Ishii, and Y. Ito, “Electrodeposition of Cu nanowire arrays with a template,” *Journal of Electroanalytical Chemistry*, vol. 559, pp. 149–153, Nov. 2003, doi: 10.1016/S0022-0728(03)00157-8.

[26] M. Arefpour, M. Almasi Kashi, F. Khansari Barzoki, M. Noormohammadi, and A. Ramazani, “Electrodeposited metal nanowires as transparent conductive electrodes: Their release conditions, electrical conductivity, optical transparency and chemical stability,” *Materials & Design*, vol. 157, pp. 326–336, Nov. 2018, doi: 10.1016/j.matdes.2018.07.048.

[27] U. S. Mohanty, “Electrodeposition: a versatile and inexpensive tool for the synthesis of nanoparticles, nanorods, nanowires, and nanoclusters of metals,” *J Appl Electrochem*, vol. 41, no. 3, pp. 257–270, Mar. 2011, doi: 10.1007/s10800-010-0234-3.

[28] H. Schlörb *et al.*, “Magnetic nanowires by electrodeposition within templates,” *physica status solidi (b)*, vol. 247, no. 10, pp. 2364–2379, 2010, doi: 10.1002/pssb.201046189.

[29] P. G. Schiavi, P. Altimari, A. Rubino, and F. Pagnanelli, “Electrodeposition of cobalt nanowires into alumina templates generated by one-step anodization,” *Electrochimica Acta*, vol. 259, pp. 711–722, Jan. 2018, doi: 10.1016/j.electacta.2017.11.035.

[30] E. Gazit, “Use of biomolecular templates for the fabrication of metal nanowires,” *The FEBS Journal*, vol. 274, no. 2, pp. 317–322, 2007, doi: 10.1111/j.1742-4658.2006.05605.x.

[31] T. Nishinaka *et al.*, “Conductive Metal Nanowires Templated by the Nucleoprotein Filaments, Complex of DNA and RecA Protein,” *J. Am. Chem. Soc.*, vol. 127, no. 22, pp. 8120–8125, Jun. 2005, doi: 10.1021/ja050487h.

[32] N. Li, Y. Shang, Z. Han, T. Wang, Z.-G. Wang, and B. Ding, “Fabrication of Metal Nanostructures on DNA Templates,” *ACS Appl. Mater. Interfaces*, vol. 11, no. 15, pp. 13835–13852, Apr. 2019, doi: 10.1021/acsami.8b16194.

[33] J. I. Mart, “Ordered magnetic nanostructures: fabrication and properties,” *Journal of Magnetism and Magnetic Materials*, p. 53, 2003.

[34] C. T. Sousa, D. C. Leitao, M. P. Proenca, J. Ventura, A. M. Pereira, and J. P. Araujo, “Nanoporous alumina as templates for multifunctional applications,” *Applied Physics Reviews*, vol. 1, no. 3, p. 031102, Sep. 2014, doi: 10.1063/1.4893546.

[35] G. Ali and M. Maqbool, “Fabrication of cobalt-nickel binary nanowires in a highly ordered alumina template via AC electrodeposition,” *Nanoscale Res Lett*, vol. 8, no. 1, p. 352, Dec. 2013, doi: 10.1186/1556-276X-8-352.

[36] J. Xu and Y. Xu, “Fabrication and magnetic property of binary Co–Ni nanowire array by alternating current electrodeposition,” *Applied Surface Science*, vol. 253, no. 17, pp. 7203–7206, Jun. 2007, doi: 10.1016/j.apsusc.2007.02.191.

[37] A. Ramazani, V. Asgari, A. H. Montazer, and M. Almasi Kashi, “Tuning magnetic fingerprints of FeNi nanowire arrays by varying length and diameter,” *Current Applied Physics*, vol. 15, no. 7, pp. 819–828, Jul. 2015, doi: 10.1016/j.cap.2015.04.023.

[38] P. Fu, G. Chen, Y. Xu, P. Cai, and X. H. Wang, “Electrodeposition and magnetic properties of ternary Fe-Co-Ni alloy nanowire arrays with high squareness ratio,” *Mater Sci-Pol*, vol. 30, no. 3, pp. 259–263, Sep. 2012, doi: 10.2478/s13536-012-0031-2.

[39] S. Kumar, A. Vohra, and S. K. Chakarvarti, “Synthesis and morphological studies of ZnCuTe ternary nanowires via template-assisted electrodeposition technique,” *J Mater Sci: Mater Electron*, vol. 23, no. 8, pp. 1485–1491, Aug. 2012, doi: 10.1007/s10854-011-0615-3.

[40] M. Jeon, T. Shimizu, and S. Shingubara, “Cu2ZnSnS4 thin films and nanowires prepared by different single-step electrodeposition method in quaternary electrolyte,” *Materials Letters*, vol. 65, no. 15–16, pp. 2364–2367, Aug. 2011, doi: 10.1016/j.matlet.2011.05.003.

[41] C. L. P. Pavithra, R. K. Siri Kiran Janardhana, K. Madhav Reddy, C. Murapaka, X. Wang, and S. R. Dey, “One-dimensional Co–Cu–Fe–Ni–Zn high-entropy alloy nanostructures,” *Materials Research Letters*, vol. 9, no. 7, pp. 285–290, Jul. 2021, doi: 10.1080/21663831.2021.1896588.

[42] K. Nguyen *et al.*, “Synthesis of Thin and Highly Conductive DNA-Based Palladium Nanowires,” *Advanced Materials*, vol. 20, no. 6, pp. 1099–1104, 2008, doi: 10.1002/adma.200701803.

[43] S. Cui, Y. Liu, Z. Yang, and X. Wei, “Construction of silver nanowires on DNA template by an electrochemical technique,” *Materials & Design*, vol. 28, no. 2, pp. 722–725, Jan. 2007, doi: 10.1016/j.matdes.2005.08.007.

[44] J. M. Slocik, S. N. Kim, T. A. Whitehead, D. S. Clark, and R. R. Naik, “Biotemplated Metal Nanowires Using Hyperthermophilic Protein Filaments,” *Small*, vol. 5, no. 18, pp. 2038–2042, 2009, doi: 10.1002/smll.200900499.

[45] J. Juárez, A. Cambón, S. Goy-López, A. Topete, P. Taboada, and V. Mosquera, “Obtention of Metallic Nanowires by Protein Biotemplating and Their Catalytic Application,” *J. Phys. Chem. Lett.*, vol. 1, no. 18, pp. 2680–2687, Sep. 2010, doi: 10.1021/jz101029f.

[46] Q. Cao, J. Li, and E. Wang, “Recent advances in the synthesis and application of copper nanomaterials based on various DNA scaffolds,” *Biosensors and Bioelectronics*, vol. 132, pp.

333–342, May 2019, doi: 10.1016/j.bios.2019.01.046.

[47] T. A. Whitehead, A. L. Meadows, and D. S. Clark, "Controlling the Self-Assembly of a Filamentous Hyperthermophilic Chaperone by an Engineered Capping Protein," *Small*, vol. 4, no. 7, pp. 956–960, 2008, doi: 10.1002/smll.200700848.

[48] T. A. Whitehead, B. B. Boonyaratanakornkit, V. Höllrigl, and D. S. Clark, "A filamentous molecular chaperone of the prefoldin family from the deep-sea hyperthermophile Methanocaldococcus jannaschii," *Protein Science*, vol. 16, no. 4, pp. 626–634, 2007, doi: 10.1110/ps.062599907.

[49] Y. Lee, J. Kim, D. S. Yun, Y. S. Nam, Y. Shao-Horn, and A. M. Belcher, "Virus-templated Au and Au–Pt core–shell nanowires and their electrocatalytic activities for fuel cell applications," *Energy Environ. Sci.*, vol. 5, no. 8, p. 8328, 2012, doi: 10.1039/c2ee21156d.

[50] S. Balci *et al.*, "Copper nanowires within the central channel of tobacco mosaic virus particles," *Electrochimica Acta*, vol. 51, no. 28, pp. 6251–6257, Sep. 2006, doi: 10.1016/j.electacta.2006.04.007.

[51] J. C. Zhou *et al.*, "Biotemplating rod-like viruses for the synthesis of copper nanorods and nanowires," *J Nanobiotechnol*, vol. 10, no. 1, p. 18, Dec. 2012, doi: 10.1186/1477-3155-10-18.

[52] H. Choi and S.-H. Park, "Seedless Growth of Free-Standing Copper Nanowires by Chemical Vapor Deposition," *J. Am. Chem. Soc.*, vol. 126, no. 20, pp. 6248–6249, May 2004, doi: 10.1021/ja049217+.

[53] J. Benson, S. Boukhalfa, A. Magasinski, A. Kvit, and G. Yushin, "Chemical Vapor Deposition of Aluminum Nanowires on Metal Substrates for Electrical Energy Storage Applications," *ACS Nano*, vol. 6, no. 1, pp. 118–125, Jan. 2012, doi: 10.1021/nn202979y.

[54] C. Kim, W. Gu, M. Briceno, I. M. Robertson, H. Choi, and K. (Kevin) Kim, "Copper Nanowires with a Five-Twinned Structure Grown by Chemical Vapor Deposition," *Advanced Materials*, vol. 20, no. 10, pp. 1859–1863, 2008, doi: 10.1002/adma.200701460.

[55] D. S. Choi, A. W. Robertson, J. H. Warner, S. O. Kim, and H. Kim, "Low-Temperature Chemical Vapor Deposition Synthesis of Pt–Co Alloyed Nanoparticles with Enhanced Oxygen Reduction Reaction Catalysis," *Advanced Materials*, vol. 28, no. 33, pp. 7115–7122, 2016, doi: 10.1002/adma.201600469.

[56] J.-M. Park, K. S. Nalwa, W. Leung, K. Constant, S. Chaudhary, and K.-M. Ho, "Fabrication of metallic nanowires and nanoribbons using laser interference lithography and shadow lithography," *Nanotechnology*, vol. 21, no. 21, p. 215301, May 2010, doi: 10.1088/0957-4484/21/21/215301.

[57] S. J. Percival, N. E. Vartanian, and B. Zhang, "Laser-pulled ultralong platinum and gold nanowires," *RSC Adv.*, vol. 4, no. 21, pp. 10491–10498, 2014, doi: 10.1039/C3RA47207H.

[58] E. B. Gordon *et al.*, "Application of Au–Cu nanowires fabricated by laser ablation in superfluid helium as catalysts for CO oxidation," *Gold Bull*, vol. 48, no. 3–4, pp. 119–125, Dec. 2015, doi: 10.1007/s13404-015-0168-y.

[59] G.-C. He *et al.*, "The Conductive Silver Nanowires Fabricated by Two-beam Laser Direct Writing on the Flexible Sheet," *Sci Rep*, vol. 7, no. 1, p. 41757, Mar. 2017, doi: 10.1038/srep41757.

[60] S. Shi *et al.*, "Fabrication of Periodic Metal Nanowires with Microscale Mold by Nanoimprint Lithography," *ACS Appl. Mater. Interfaces*, vol. 3, no. 11, pp. 4174–4179, Nov. 2011, doi: 10.1021/am2010338.

[61] V. Auzelyte *et al.*, “Large area arrays of metal nanowires,” *Microelectronic Engineering*, vol. 85, no. 5–6, pp. 1131–1134, May 2008, doi: 10.1016/j.mee.2008.01.064.

[62] Y.-J. Chen, J.-H. Hsu, and H.-N. Lin, “Fabrication of metal nanowires by atomic force microscopy nanoscratching and lift-off process,” *Nanotechnology*, vol. 16, no. 8, pp. 1112–1115, Aug. 2005, doi: 10.1088/0957-4484/16/8/020.

[63] Q. Xie, M. H. Hong, H. L. Tan, G. X. Chen, L. P. Shi, and T. C. Chong, “Fabrication of nanostructures with laser interference lithography,” *Journal of Alloys and Compounds*, vol. 449, no. 1–2, pp. 261–264, Jan. 2008, doi: 10.1016/j.jallcom.2006.02.115.

[64] S. Hong *et al.*, “Highly Stretchable and Transparent Metal Nanowire Heater for Wearable Electronics Applications,” *Adv. Mater.*, vol. 27, no. 32, pp. 4744–4751, Aug. 2015, doi: 10.1002/adma.201500917.

[65] B. Cui and T. Veres, “Fabrication of metal nanoring array by nanoimprint lithography (NIL) and reactive ion etching,” *Microelectronic Engineering*, vol. 84, no. 5–8, pp. 1544–1547, May 2007, doi: 10.1016/j.mee.2007.01.158.

[66] H.-W. Yoo, J.-M. Jung, S. Lee, and H.-T. Jung, “The fabrication of highly ordered silver nanodot patterns by platinum assisted nanoimprint lithography,” *Nanotechnology*, vol. 22, no. 9, p. 095304, Mar. 2011, doi: 10.1088/0957-4484/22/9/095304.

[67] J.-H. Lee, K. Yang, S.-H. Hong, H. Lee, and K.-W. Choi, “Fabrication of 70nm narrow metal nanowire structure on flexible PET film by nanoimprint lithography,” *Microelectronic Engineering*, vol. 85, no. 4, pp. 710–713, Apr. 2008, doi: 10.1016/j.mee.2007.12.058.

[68] S. Shi *et al.*, “Fabrication of Periodic Metal Nanowires with Microscale Mold by Nanoimprint Lithography,” *ACS Appl. Mater. Interfaces*, vol. 3, no. 11, pp. 4174–4179, Nov. 2011, doi: 10.1021/am2010338.

[69] J.-Y. Lee, S. T. Connor, Y. Cui, and P. Peumans, “Solution-Processed Metal Nanowire Mesh Transparent Electrodes,” *Nano Lett.*, vol. 8, no. 2, pp. 689–692, Feb. 2008, doi: 10.1021/nl073296g.

[70] T. Sannicolo, M. Lagrange, A. Cabos, C. Celle, J.-P. Simonato, and D. Bellet, “Metallic Nanowire-Based Transparent Electrodes for Next Generation Flexible Devices: a Review,” *Small*, vol. 12, no. 44, pp. 6052–6075, 2016, doi: 10.1002/smll.201602581.

[71] S. Huang, Y. Liu, F. Yang, Y. Wang, T. Yu, and D. Ma, “Recent advances of metal nanowire based transparent conductive electrodes for flexible chromatic devices,” In Review, preprint, Feb. 2022. doi: 10.21203/rs.3.rs-1264154/v1.

[72] M. Z. Atashbar and S. Singamaneni, “Room temperature gas sensor based on metallic nanowires,” *Sensors and Actuators B: Chemical*, vol. 111–112, pp. 13–21, Nov. 2005, doi: 10.1016/j.snb.2005.07.034.

[73] T. Araki *et al.*, “Wireless Monitoring Using a Stretchable and Transparent Sensor Sheet Containing Metal Nanowires,” *Adv. Mater.*, vol. 32, no. 15, p. 1902684, Apr. 2020, doi: 10.1002/adma.201902684.

[74] S. Lal, J. H. Hafner, N. J. Halas, S. Link, and P. Nordlander, “Noble Metal Nanowires: From Plasmon Waveguides to Passive and Active Devices,” *Acc. Chem. Res.*, vol. 45, no. 11, pp. 1887–1895, Nov. 2012, doi: 10.1021/ar300133j.

[75] A. Cao, “Shape memory effects and pseudoelasticity in bcc metallic nanowires,” *Journal of*

*Applied Physics*, vol. 108, no. 11, p. 113531, Dec. 2010, doi: 10.1063/1.3506413.

[76] W. Liang and M. Zhou, “Atomistic simulations reveal shape memory of fcc metal nanowires,” *Phys. Rev. B*, vol. 73, no. 11, Art. no. 11, Mar. 2006, doi: 10.1103/PhysRevB.73.115409.

[77] R. Rezaei and C. Deng, “Pseudoelasticity and shape memory effects in cylindrical FCC metal nanowires,” *Acta Materialia*, vol. 132, pp. 49–56, Jun. 2017, doi: 10.1016/j.actamat.2017.04.039.

[78] M. García, P. Batalla, and A. Escarpa, “Metallic and polymeric nanowires for electrochemical sensing and biosensing,” *TrAC Trends in Analytical Chemistry*, vol. 57, pp. 6–22, May 2014, doi: 10.1016/j.trac.2014.01.004.

[79] R. M. Penner, “A Nose for Hydrogen Gas: Fast, Sensitive $H_2$ Sensors Using Electrodeposited Nanomaterials,” *Acc. Chem. Res.*, vol. 50, no. 8, pp. 1902–1910, Aug. 2017, doi: 10.1021/acs.accounts.7b00163.

[80] K. K. Kim *et al.*, “Highly Sensitive and Stretchable Multidimensional Strain Sensor with Prestrained Anisotropic Metal Nanowire Percolation Networks,” *Nano Lett.*, vol. 15, no. 8, pp. 5240–5247, Aug. 2015, doi: 10.1021/acs.nanolett.5b01505.

[81] W. Liang, M. Zhou, and F. Ke, “Shape Memory Effect in Cu Nanowires,” *Nano Lett.*, vol. 5, no. 10, pp. 2039–2043, Oct. 2005, doi: 10.1021/nl0515910.

[82] W. D. Callister and D. G. Rethwisch, *Materials science and engineering: an introduction*, vol. 9. Wiley New York, 2018.

[83] “Stress–strain curve,” *Wikipedia*. Sep. 08, 2022. Accessed: Sep. 14, 2022. [Online]. Available: https://en.wikipedia.org/w/index.php?title=Stress%E2%80%93strain_curve&oldid=1109114252

[84] Y. Zhu *et al.*, “Size effects on elasticity, yielding, and fracture of silver nanowires: *In situ* experiments,” *Phys. Rev. B*, vol. 85, no. 4, Art. no. 4, Jan. 2012, doi: 10.1103/PhysRevB.85.045443.

[85] Y. Zhu, F. Xu, Q. Qin, W. Y. Fung, and W. Lu, “Mechanical Properties of Vapor−Liquid−Solid Synthesized Silicon Nanowires,” *Nano Lett.*, vol. 9, no. 11, pp. 3934–3939, Nov. 2009, doi: 10.1021/nl902132w.

[86] F. Xu, Q. Qin, A. Mishra, Y. Gu, and Y. Zhu, “Mechanical properties of ZnO nanowires under different loading modes,” *Nano Res.*, vol. 3, no. 4, pp. 271–280, Apr. 2010, doi: 10.1007/s12274-010-1030-4.

[87] B. Wu, A. Heidelberg, and J. J. Boland, “Mechanical properties of ultrahigh-strength gold nanowires,” *Nature Mater*, vol. 4, no. 7, Art. no. 7, Jul. 2005, doi: 10.1038/nmat1403.

[88] H. W. P. Koops, “Fabrication and characterization of platinum nanocrystalline material grown by electron-beam induced deposition,” *J. Vac. Sci. Technol. B*, vol. 13, no. 6, p. 2400, Nov. 1995, doi: 10.1116/1.588008.

[89] A. P. Thompson, “LAMMPS - a flexible simulation tool for particle-based materials modeling at the atomic, meso, and continuum scales,” *Computer Physics Communications*, p. 34, 2022.

[90] C. Deng and F. Sansoz, “Size-dependent yield stress in twinned gold nanowires mediated by site-specific surface dislocation emission,” *Appl. Phys. Lett.*, vol. 95, no. 9, p. 091914, Aug. 2009, doi: 10.1063/1.3222936.

[91] S. Narayanan, G. Cheng, Z. Zeng, Y. Zhu, and T. Zhu, “Strain Hardening and Size Effect in Five-fold Twinned Ag Nanowires,” *Nano Lett.*, vol. 15, no. 6, pp. 4037–4044, Jun. 2015, doi: 10.1021/acs.nanolett.5b01015.

[92] V. Guder and S. Sengul, “Tensile strength and failure mechanism of hcp zirconium nanowires: Effect of diameter, temperature and strain rate,” *Computational Materials Science*, vol. 177, p. 109551, May 2020, doi: 10.1016/j.commatsci.2020.109551.

[93] H. Ikeda, Y. Qi, T. Çagin, K. Samwer, W. L. Johnson, and W. A. Goddard, “Strain Rate Induced Amorphization in Metallic Nanowires,” *Phys. Rev. Lett.*, vol. 82, no. 14, pp. 2900–2903, Apr. 1999, doi: 10.1103/PhysRevLett.82.2900.

[94] S. K. R. S. Sankaranarayanan, V. R. Bhethanabotla, and B. Joseph, “Molecular dynamics simulation of temperature and strain rate effects on the elastic properties of bimetallic Pd-Pt nanowires,” *Phys. Rev. B*, vol. 76, no. 13, Art. no. 13, Oct. 2007, doi: 10.1103/PhysRevB.76.134117.

[95] Y.-H. Wen, Z.-Z. Zhu, and R.-Z. Zhu, “Molecular dynamics study of the mechanical behavior of nickel nanowire: Strain rate effects,” *Computational Materials Science*, vol. 41, no. 4, Art. no. 4, Feb. 2008, doi: 10.1016/j.commatsci.2007.05.012.

[96] L. Chang, C.-Y. Zhou, H.-X. Liu, J. Li, and X.-H. He, “Orientation and strain rate dependent tensile behavior of single crystal titanium nanowires by molecular dynamics simulations,” *Journal of Materials Science & Technology*, vol. 34, no. 5, pp. 864–877, May 2018, doi: 10.1016/j.jmst.2017.03.011.

[97] H. S. Park, K. Gall, and J. A. Zimmerman, “Deformation of FCC nanowires by twinning and slip,” *Journal of the Mechanics and Physics of Solids*, vol. 54, no. 9, pp. 1862–1881, Sep. 2006, doi: 10.1016/j.jmps.2006.03.006.

[98] P. Rohith, G. Sainath, and B. K. Choudhary, “Effect of orientation and mode of loading on deformation behaviour of Cu nanowires,” *Computational Condensed Matter*, vol. 17, p. e00330, Dec. 2018, doi: 10.1016/j.cocom.2018.e00330.

[99] H.-K. Kim, S.-H. Kim, J.-P. Ahn, and J.-C. Lee, “Deformation criterion for face-centered-cubic metal nanowires,” *Materials Science and Engineering: A*, vol. 736, pp. 431–437, Oct. 2018, doi: 10.1016/j.msea.2018.08.108.

[100] S. Yin, G. Cheng, G. Richter, H. Gao, and Y. Zhu, “Transition of Deformation Mechanisms in Single-Crystalline Metallic Nanowires,” *ACS Nano*, vol. 13, no. 8, pp. 9082–9090, Aug. 2019, doi: 10.1021/acsnano.9b03311.

[101] S. J. A. Koh and H. P. Lee, “Molecular dynamics simulation of size and strain rate dependent mechanical response of FCC metallic nanowires,” *Nanotechnology*, vol. 17, no. 14, pp. 3451–3467, Jul. 2006, doi: 10.1088/0957-4484/17/14/018.

[102] H. Xie, F. Yin, T. Yu, G. Lu, and Y. Zhang, “A new strain-rate-induced deformation mechanism of Cu nanowire: Transition from dislocation nucleation to phase transformation,” *Acta Materialia*, vol. 85, pp. 191–198, Feb. 2015, doi: 10.1016/j.actamat.2014.11.017.

[103] P. Wang, W. Chou, A. Nie, Y. Huang, H. Yao, and H. Wang, “Molecular dynamics simulation on deformation mechanisms in body-centered-cubic molybdenum nanowires,” *Journal of Applied Physics*, vol. 110, no. 9, p. 093521, Nov. 2011, doi: 10.1063/1.3660251.

[104] G. Sainath and B. K. Choudhary, “Twinning to slip transition in ultrathin BCC Fe nanowires,” *Physics Letters A*, vol. 382, no. 15, pp. 1047–1051, Apr. 2018, doi: 10.1016/j.physleta.2018.02.007.

[105] G. Sainath and B. K. Choudhary, “Molecular dynamics simulations on size dependent tensile

deformation behaviour of [110] oriented body centred cubic iron nanowires," *Materials Science and Engineering: A*, vol. 640, pp. 98–105, Jul. 2015, doi: 10.1016/j.msea.2015.05.084.

[106] X. Li, W. Hu, S. Xiao, and W.-Q. Huang, "Stress-induced phase transformation and strain rate effect in polycrystalline Mo nanowires," *Physica E: Low-dimensional Systems and Nanostructures*, vol. 43, no. 5, pp. 1131–1139, Mar. 2011, doi: 10.1016/j.physe.2011.01.017.

[107] H. Xie, T. Yu, W. Fang, F. Yin, and D. F. Khan, "Strain-rate-induced bcc-to-hcp phase transformation of Fe nanowires," *Chinese Phys. B*, vol. 25, no. 12, p. 126201, Dec. 2016, doi: 10.1088/1674-1056/25/12/126201.

[108] Z. Shi and C. V. Singh, "Competing twinning mechanisms in body-centered cubic metallic nanowires," *Scripta Materialia*, vol. 113, pp. 214–217, Mar. 2016, doi: 10.1016/j.scriptamat.2015.11.006.

[109] J. S. Lehtinen, K. Zakharov, and K. Yu. Arutyunov, "Coulomb Blockade and Bloch Oscillations in Superconducting Ti Nanowires," *Phys. Rev. Lett.*, vol. 109, no. 18, p. 187001, Oct. 2012, doi: 10.1103/PhysRevLett.109.187001.

[110] X. Han *et al.*, "Influence of crystal orientation on magnetic properties of hcp Co nanowire arrays," *J. Phys. D: Appl. Phys.*, vol. 42, no. 9, p. 095005, May 2009, doi: 10.1088/0022-3727/42/9/095005.

[111] Yu. P. Ivanov, L. G. Vivas, A. Asenjo, A. Chuvilin, O. Chubykalo-fesenko, and M. Vázquez, "Magnetic structure of a single-crystal hcp electrodeposited cobalt nanowire," *EPL*, vol. 102, no. 1, p. 17009, Apr. 2013, doi: 10.1209/0295-5075/102/17009.

[112] L. Chang, C.-Y. Zhou, X.-M. Pan, and X.-H. He, "Size-dependent deformation mechanism transition in titanium nanowires under high strain rate tension," *Materials & Design*, vol. 134, pp. 320–330, Nov. 2017, doi: 10.1016/j.matdes.2017.08.058.

[113] L. Chang, C.-Y. Zhou, L.-L. Wen, J. Li, and X.-H. He, "Molecular dynamics study of strain rate effects on tensile behavior of single crystal titanium nanowire," *Computational Materials Science*, vol. 128, pp. 348–358, Feb. 2017, doi: 10.1016/j.commatsci.2016.11.034.

[114] J. Weissmiiller, "ALLOY EFFECTS IN NANOSTRUCTURES," p. 12.

[115] R. J. Arsenault, "Solid solution strengthening and weakening of b.c.c. solid solutions," *Acta Metallurgica*, vol. 17, no. 10, pp. 1291–1297, Oct. 1969, doi: 10.1016/0001-6160(69)90144-8.

[116] R. L. Fleisgher, "Solution hardening," *Acta metallurgica*, vol. 9, no. 11, pp. 996–1000, 1961.

[117] R. L. Fleischer, "Substitutional solution hardening," *Acta metallurgica*, vol. 11, no. 3, pp. 203–209, 1963.

[118] R. Labusch, "A Statistical Theory of Solid Solution Hardening," *phys. stat. sol. (b)*, vol. 41, no. 2, Art. no. 2, 1970, doi: 10.1002/pssb.19700410221.

[119] R. Labusch, "Statistical theories of solid solution hardening(Concentration of solute atoms, interaction range between solute atoms and distortion, and interaction strength of solid solution hardening)," *Acta Met.,(London)*, vol. 20, pp. 917–927, 1972.

[120] M. Ames, J. Markmann, R. Karos, A. Michels, A. Tschöpe, and R. Birringer, "Unraveling the nature of room temperature grain growth in nanocrystalline materials," *Acta Materialia*, vol. 56, no. 16, pp. 4255–4266, Sep. 2008, doi: 10.1016/j.actamat.2008.04.051.

[121] M. Jin, A. M. Minor, E. A. Stach, and J. W. Morris, "Direct observation of deformation-induced grain growth during the nanoindentation of ultrafine-grained Al at room temperature," *Acta*

*Materialia*, vol. 52, no. 18, pp. 5381–5387, Oct. 2004, doi: 10.1016/j.actamat.2004.07.044.

[122] T. J. Rupert, J. C. Trenkle, and C. A. Schuh, “Enhanced solid solution effects on the strength of nanocrystalline alloys,” *Acta Materialia*, vol. 59, no. 4, Art. no. 4, Feb. 2011, doi: 10.1016/j.actamat.2010.11.026.

[123] T. J. Rupert, “Solid solution strengthening and softening due to collective nanocrystalline deformation physics,” *Scripta Materialia*, vol. 81, pp. 44–47, Jun. 2014, doi: 10.1016/j.scriptamat.2014.03.006.

[124] X. Zhang, H. Deng, S. Xiao, X. Li, and W. Hu, “Atomistic simulations of solid solution strengthening in Ni-based superalloy,” *Computational Materials Science*, vol. 68, pp. 132–137, Feb. 2013, doi: 10.1016/j.commatsci.2012.10.002.

[125] B. Cantor, I. T. H. Chang, P. Knight, and A. J. B. Vincent, “Microstructural development in equiatomic multicomponent alloys,” *Materials Science and Engineering: A*, vol. 375–377, pp. 213–218, Jul. 2004, doi: 10.1016/j.msea.2003.10.257.

[126] J. Y. He *et al.*, “Effects of Al addition on structural evolution and tensile properties of the FeCoNiCrMn high-entropy alloy system,” *Acta Materialia*, vol. 62, pp. 105–113, Jan. 2014, doi: 10.1016/j.actamat.2013.09.037.

[127] J. Kumar, A. Linda, M. Sadhasivam, K. G. Pradeep, N. P. Gurao, and K. Biswas, “The Effect of Al Addition on Solid Solution Strengthening in CoCrFeMnNi: Experiment and Modelling,” *Acta Materialia*, p. 118208, Jul. 2022, doi: 10.1016/j.actamat.2022.118208.

[128] H. Oh *et al.*, “Lattice Distortions in the FeCoNiCrMn High Entropy Alloy Studied by Theory and Experiment,” *Entropy*, vol. 18, no. 9, p. 321, Sep. 2016, doi: 10.3390/e18090321.

[129] L. R. Owen, E. J. Pickering, H. Y. Playford, H. J. Stone, M. G. Tucker, and N. G. Jones, “An assessment of the lattice strain in the CrMnFeCoNi high-entropy alloy,” *Acta Materialia*, vol. 122, pp. 11–18, Jan. 2017, doi: 10.1016/j.actamat.2016.09.032.

[130] Z. Wang, Q. Fang, J. Li, B. Liu, and Y. Liu, “Effect of lattice distortion on solid solution strengthening of BCC high-entropy alloys,” *Journal of Materials Science & Technology*, vol. 34, no. 2, pp. 349–354, Feb. 2018, doi: 10.1016/j.jmst.2017.07.013.

[131] F. G. Coury, “Solid-solution strengthening in refractory high entropy alloys,” *Acta Materialia*, p. 16, 2019.

[132] C. Lee *et al.*, “Lattice-Distortion-Enhanced Yield Strength in a Refractory High-Entropy Alloy,” *Advanced Materials*, vol. 32, no. 49, p. 2004029, 2020, doi: 10.1002/adma.202004029.

[133] C. Lee *et al.*, “Lattice distortion in a strong and ductile refractory high-entropy alloy,” *Acta Materialia*, vol. 160, pp. 158–172, Nov. 2018, doi: 10.1016/j.actamat.2018.08.053.

[134] Z. An *et al.*, “A novel HfNbTaTiV high-entropy alloy of superior mechanical properties designed on the principle of maximum lattice distortion,” *Journal of Materials Science & Technology*, vol. 79, pp. 109–117, Jul. 2021, doi: 10.1016/j.jmst.2020.10.073.

[135] R. J. Arsenault, “The double-kink model for low-temperature deformation of B.C.C. metals and solid solutions,” *Acta Metallurgica*, vol. 15, no. 3, pp. 501–511, Mar. 1967, doi: 10.1016/0001-6160(67)90083-1.

[136] N. I. Medvedeva, Yu. N. Gornostyrev, and A. J. Freeman, “Electronic Origin of Solid Solution Softening in bcc Molybdenum Alloys,” *Phys. Rev. Lett.*, vol. 94, no. 13, p. 136402, Apr. 2005, doi: 10.1103/PhysRevLett.94.136402.

[137] N. I. Medvedeva, Yu. N. Gornostyrev, and A. J. Freeman, “Solid solution softening in bcc Mo alloys: Effect of transition-metal additions on dislocation structure and mobility,” *Phys. Rev. B*, vol. 72, no. 13, p. 134107, Oct. 2005, doi: 10.1103/PhysRevB.72.134107.

[138] N. I. Medvedeva, Yu. N. Gornostyrev, and A. J. Freeman, “Solid solution softening and hardening in the group-V and group-VI bcc transition metals alloys: First principles calculations and atomistic modeling,” *Phys. Rev. B*, vol. 76, no. 21, p. 212104, Dec. 2007, doi: 10.1103/PhysRevB.76.212104.

[139] Q. Cheng, X. D. Xu, X. Q. Li, Y. P. Li, T. G. Nieh, and M. W. Chen, “Solid solution softening in a Al0.1CoCrFeMnNi high-entropy alloy,” *Scripta Materialia*, vol. 186, pp. 63–68, Sep. 2020, doi: 10.1016/j.scriptamat.2020.04.034.

[140] A. Bisht, R. K. Koju, Y. Qi, J. Hickman, Y. Mishin, and E. Rabkin, “The impact of alloying on defect-free nanoparticles exhibiting softer but tougher behavior,” *Nat Commun*, vol. 12, no. 1, Art. no. 1, Dec. 2021, doi: 10.1038/s41467-021-22707-x.

[141] Y.-J. Hu *et al.*, “Solute-induced solid-solution softening and hardening in bcc tungsten,” *Acta Materialia*, vol. 141, pp. 304–316, Dec. 2017, doi: 10.1016/j.actamat.2017.09.019.

[142] J. Chen, P. Li, and E. E. Lin, “A molecular dynamics study on the mechanical properties of Fe–Ni alloy nanowires and their temperature dependence,” *RSC Adv.*, vol. 10, no. 66, Art. no. 66, 2020, doi: 10.1039/D0RA07831J.

[143] Y. Huo, J. Wu, and C. C. Lee, “Solid solution softening and enhanced ductility in concentrated FCC silver solid solution alloys,” *Materials Science and Engineering: A*, vol. 729, pp. 208–218, Jun. 2018, doi: 10.1016/j.msea.2018.05.057.

[144] T. Tsuru, Y. Udagawa, M. Yamaguchi, M. Itakura, H. Kaburaki, and Y. Kaji, “Solution softening in magnesium alloys: the effect of solid solutions on the dislocation core structure and nonbasal slip,” *J. Phys.: Condens. Matter*, vol. 25, no. 2, p. 022202, Jan. 2013, doi: 10.1088/0953-8984/25/2/022202.

[145] D. Frenkel and B. Smit, *Understanding molecular simulation: from algorithms to applications*, vol. 1. Elsevier, 2001.

[146] P. Hirel, “Atomsk: A tool for manipulating and converting atomic data files,” *Computer Physics Communications*, vol. 197, pp. 212–219, Dec. 2015, doi: 10.1016/j.cpc.2015.07.012.

[147] A. Stukowski, “Visualization and analysis of atomistic simulation data with OVITO–the Open Visualization Tool,” *Modelling Simul. Mater. Sci. Eng.*, vol. 18, no. 1, p. 015012, Jan. 2010, doi: 10.1088/0965-0393/18/1/015012.

[148] D. Faken and H. Jónsson, “Systematic analysis of local atomic structure combined with 3D computer graphics,” *Computational Materials Science*, vol. 2, no. 2, pp. 279–286, Mar. 1994, doi: 10.1016/0927-0256(94)90109-0.

[149] A. Stukowski, V. V. Bulatov, and A. Arsenlis, “Automated identification and indexing of dislocations in crystal interfaces,” *Modelling Simul. Mater. Sci. Eng.*, vol. 20, no. 8, p. 085007, Dec. 2012, doi: 10.1088/0965-0393/20/8/085007.

[150] R. Giraud *et al.*, “Strain Effect on the $\gamma'$ Dissolution at High Temperatures of a Nickel-Based Single Crystal Superalloy,” *Metall and Mat Trans A*, vol. 44, no. 1, pp. 131–146, Jan. 2013, doi: 10.1007/s11661-012-1397-9.

[151] H. Sun, J. Wang, Z. Li, P. Zhang, and X. Su, “Corrosion behavior of 316SS and Ni-based alloys

in a ternary NaCl-KCl-MgCl2 molten salt," *Solar Energy*, vol. 171, pp. 320–329, Sep. 2018, doi: 10.1016/j.solener.2018.06.094.

[152] J. Liu, H. Liu, X. Tian, H. Yang, and J. Hao, "Microstructural evolution and corrosion properties of Ni-based alloy coatings fabricated by multi-layer laser cladding on cast iron," *Journal of Alloys and Compounds*, vol. 822, p. 153708, May 2020, doi: 10.1016/j.jallcom.2020.153708.

[153] Z. Wu, Y.-W. Zhang, M. H. Jhon, H. Gao, and D. J. Srolovitz, "Nanowire Failure: Long = Brittle and Short = Ductile," *Nano Lett.*, vol. 12, no. 2, Art. no. 2, Feb. 2012, doi: 10.1021/nl203980u.

[154] A. Shirinyan, M. Wautelet, and Y. Belogorodsky, "Solubility diagram of the Cu–Ni nanosystem," *J. Phys.: Condens. Matter*, vol. 18, no. 8, pp. 2537–2551, Mar. 2006, doi: 10.1088/0953-8984/18/8/016.

[155] T. Nishizawa and K. Ishida, "The Co (Cobalt) system," *Bulletin of Alloy Phase Diagrams*, vol. 4, no. 4, pp. 387–390, Dec. 1983, doi: 10.1007/BF02868089.

[156] B. Onat and S. Durukanoğlu, "An optimized interatomic potential for Cu–Ni alloys with the embedded-atom method," *J. Phys.: Condens. Matter*, vol. 26, no. 3, p. 035404, Jan. 2014, doi: 10.1088/0953-8984/26/3/035404.

[157] G. P. Purja Pun, V. Yamakov, and Y. Mishin, "Interatomic potential for the ternary Ni–Al–Co system and application to atomistic modeling of the B2–L1$_0$ martensitic transformation," *Modelling Simul. Mater. Sci. Eng.*, vol. 23, no. 6, Art. no. 6, Sep. 2015, doi: 10.1088/0965-0393/23/6/065006.

[158] O. R. Deluigi, R. C. Pasianot, F. J. Valencia, A. Caro, D. Farkas, and E. M. Bringa, "Simulations of primary damage in a High Entropy Alloy: Probing enhanced radiation resistance," *Acta Materialia*, vol. 213, p. 116951, Jul. 2021, doi: 10.1016/j.actamat.2021.116951.

[159] Y.-K. Kim, W.-S. Jung, and B.-J. Lee, "Modified embedded-atom method interatomic potentials for the Ni–Co binary and the Ni–Al–Co ternary systems," *Modelling Simul. Mater. Sci. Eng.*, vol. 23, no. 5, p. 055004, Jul. 2015, doi: 10.1088/0965-0393/23/5/055004.

[160] D. H. Tsai, "The virial theorem and stress calculation in molecular dynamics," *The Journal of Chemical Physics*, vol. 70, no. 3, pp. 1375–1382, Feb. 1979, doi: 10.1063/1.437577.

[161] P. L. Williams, Y. Mishin, and J. C. Hamilton, "An embedded-atom potential for the Cu–Ag system," *Modelling Simul. Mater. Sci. Eng.*, vol. 14, no. 5, pp. 817–833, Jul. 2006, doi: 10.1088/0965-0393/14/5/002.

[162] J. A. Zimmerman, H. Gao, and F. F. Abraham, "Generalized stacking fault energies for embedded atom FCC metals," *Modelling Simul. Mater. Sci. Eng.*, vol. 8, no. 2, pp. 103–115, Mar. 2000, doi: 10.1088/0965-0393/8/2/302.

[163] C. Deng and F. Sansoz, "Fundamental differences in the plasticity of periodically twinned nanowires in Au, Ag, Al, Cu, Pb and Ni," *Acta Materialia*, vol. 57, no. 20, pp. 6090–6101, Dec. 2009, doi: 10.1016/j.actamat.2009.08.035.

[164] J. Xiao and C. Deng, "Continuous strengthening in nanotwinned high-entropy alloys enabled by martensite transformation," *Phys. Rev. Materials*, vol. 4, no. 4, p. 043602, Apr. 2020, doi: 10.1103/PhysRevMaterials.4.043602.

[165] B. Sadigh, P. Erhart, A. Stukowski, A. Caro, E. Martinez, and L. Zepeda-Ruiz, "Scalable parallel Monte Carlo algorithm for atomistic simulations of precipitation in alloys," *Phys. Rev. B*, vol. 85, no. 18, p. 184203, May 2012, doi: 10.1103/PhysRevB.85.184203.

[166] S. J. Kim, E. A. Stach, and C. A. Handwerker, “Fabrication of conductive interconnects by Ag migration in Cu–Ag core-shell nanoparticles,” *Appl. Phys. Lett.*, vol. 96, no. 14, p. 144101, Apr. 2010, doi: 10.1063/1.3364132.

[167] I. E. Stewart, S. Ye, Z. Chen, P. F. Flowers, and B. J. Wiley, “Synthesis of Cu–Ag, Cu–Au, and Cu–Pt Core–Shell Nanowires and Their Use in Transparent Conducting Films,” *Chem. Mater.*, vol. 27, no. 22, pp. 7788–7794, Nov. 2015, doi: 10.1021/acs.chemmater.5b03709.

[168] S. Sompech, S. Thaomola, A. Chingsungnoen, and T. Dasri, “Theoretical calculation of optical absorption property of Cu@Ag core–shell composite nanoparticle,” *Mater. Res. Express*, vol. 6, no. 2, p. 026201, Nov. 2018, doi: 10.1088/2053-1591/aaeb58.

[169] M. I. Mendelev, M. Asta, M. J. Rahman, and J. J. Hoyt, “Development of interatomic potentials appropriate for simulation of solid–liquid interface properties in Al–Mg alloys,” *Philosophical Magazine*, vol. 89, no. 34–36, pp. 3269–3285, Dec. 2009, doi: 10.1080/14786430903260727.

[170] Dr. D. Caillard, “A TEM in situ study of the softening of Tungsten by Rhenium,” *Acta Materialia*, vol. 194, pp. 249–256, Aug. 2020, doi: 10.1016/j.actamat.2020.04.039.

[171] C. Ren, Z. Z. Fang, M. Koopman, B. Butler, J. Paramore, and S. Middlemas, “Methods for improving ductility of tungsten - A review,” *International Journal of Refractory Metals and Hard Materials*, vol. 75, pp. 170–183, Sep. 2018, doi: 10.1016/j.ijrmhm.2018.04.012.

[172] A. Datta, Z. Duan, and G. Wang, “Influence of surface segregation on the elastic property of Pt–Ni alloy nanowires,” *Computational Materials Science*, vol. 55, pp. 81–84, Apr. 2012, doi: 10.1016/j.commatsci.2011.12.017.

[173] L. Wei, W. Qi, B. Huang, and M. Wang, “Surface segregation of Au–Ag bimetallic nanowires,” *Computational Materials Science*, vol. 69, pp. 374–380, Mar. 2013, doi: 10.1016/j.commatsci.2012.11.038.

[174] S. Shetty, M. Gayen, S. Agarwal, D. Chatterjee, A. Singh, and N. Ravishankar, “Tuning Catalytic Activity in Ultrathin Bimetallic Nanowires via Surface Segregation: Some Insights,” *J. Phys. Chem. Lett.*, vol. 13, no. 3, pp. 770–776, Jan. 2022, doi: 10.1021/acs.jpclett.1c03852.

[175] M. S. Nitol, S. Adibi, C. D. Barrett, and J. W. Wilkerson, “Solid solution softening in dislocation-starved Mg–Al alloys,” *Mechanics of Materials*, vol. 150, p. 103588, Nov. 2020, doi: 10.1016/j.mechmat.2020.103588.

[176] Y. Zhang, X. Yang, and P. K. Liaw, “Alloy Design and Properties Optimization of High-Entropy Alloys,” *JOM*, vol. 64, no. 7, pp. 830–838, Jul. 2012, doi: 10.1007/s11837-012-0366-5.

[177] N. N. Greenwood and A. Earnshaw, *Chemistry of the Elements*. Elsevier, 2012.